

Spiral instability-modes on rotating cones in high-Reynolds number axial flow

Tambe, S.S.; Schrijer, F.F.J.; Veldhuis, L.L.M.; Gangoli Rao, A.

DOI

[10.1063/5.0083564](https://doi.org/10.1063/5.0083564)

Publication date

2022

Document Version

Accepted author manuscript

Published in

Physics of Fluids

Citation (APA)

Tambe, S. S., Schrijer, F. F. J., Veldhuis, L. L. M., & Gangoli Rao, A. (2022). Spiral instability-modes on rotating cones in high-Reynolds number axial flow. *Physics of Fluids*, 34(3), Article 034109. <https://doi.org/10.1063/5.0083564>

Important note

To cite this publication, please use the final published version (if applicable). Please check the document version above.

Copyright

Other than for strictly personal use, it is not permitted to download, forward or distribute the text or part of it, without the consent of the author(s) and/or copyright holder(s), unless the work is under an open content license such as Creative Commons.

Takedown policy

Please contact us and provide details if you believe this document breaches copyrights. We will remove access to the work immediately and investigate your claim.

Spiral instability-modes on rotating cones in high-Reynolds-number axial flow

Sumit Tambe,¹ Ferry Schrijer,¹ Leo Veldhuis,¹ and Arvind Gangoli Rao¹
 AWEF, Aerospace Engineering, Delft University of Technology, Klyuwerweg-1, 2629HS Delft,
 The Netherlands

(*Electronic mail: A.GangoliRao@tudelft.nl)

(*Electronic mail: L.L.M.Veldhuis@tudelft.nl)

(*Electronic mail: F.F.J.Schrijer@tudelft.nl)

(*Electronic mail: S.S.Tambe@tudelft.nl)

(Dated: 17 February 2022)

This work shows the behaviour of an unstable boundary-layer on rotating cones in *high-speed* flow conditions: high Reynolds number $Re_l > 10^6$, low rotational speed ratio $S < 1-1.5$, and inflow Mach number $M = 0.5$. These conditions are most-commonly encountered on rotating aero-engine-nose-cones of transonic cruise aircraft. Although it has been addressed in several past studies, the boundary-layer instability on rotating cones remained to be explored in *high-speed* inflow regime. This work uses infrared-thermography with POD approach to detect instability-induced flow structures by measuring their thermal footprints on rotating cones in *high-speed* inflow. Observed surface temperature patterns show that the boundary-layer instability induces spiral modes on rotating cones, which closely resemble the thermal footprints of the spiral vortices observed in the past studies at *low-speed* flow conditions: $Re_l < 10^5$, $S > 1$, and $M \approx 0$. Three cones with half-cone angles $\psi = 15^\circ$, 30° , and 40° are tested. For a given cone, the Reynolds number relating to the maximum amplification of the spiral vortices is found to follow an exponential relation with the rotational speed ratio S , extending from *low-* to *high-speed* regime. At a given rotational speed ratio S , the spiral vortex angle appears to be as expected from the *low-speed* studies, irrespective of the half-cone angle.

I. INTRODUCTION

Instability and transition of the rotating boundary-layers has classically been a subject of great interest due to its abundance in nature (rotating planets, stars, etc.) and in industry (turbo-machinery, wheels, rotating projectiles, etc.). Depending on the geometry, centrifugal or cross-flow instability gives rise to coherent spiral vortices in an unstable laminar boundary-layer on a rotating body, e.g. disk, cone, and sphere. Upon their spatial growth, the vortices alter the basic boundary-layer profile by enhancing the mixing of high- and low-momentum flow, and subsequently, lead the boundary-layer towards a turbulent state^{1,2}.

Investigating this transition process is important for efficiency improvements in engineering applications. For example, in compressor cascades, the state (laminar/turbulent) of the hub end-wall boundary-layer influences the aerodynamic losses³. In aero-engines, the hub-end-wall boundary-layer begins right from the tip of a rotating nose-cone. Here, accurately assessing the aerodynamic losses in engine components (fan and compressors) requires knowing the instability behaviour of the rotating nose-cone boundary-layer.

In the past, instability mechanisms in rotating boundary-layer flows were first discovered through studies on a disk rotating in still fluid. One of the first experiments by Smith⁴ showed that the laminar boundary layer over a rotating disk exhibits sinusoidal velocity fluctuations, before transitioning into a fully turbulent state. Later on, the experiments of Gregory, Stuart, and Walker⁵ revealed that these velocity fluctuations are due to the spiral vortices formed near the rotating disk surface. Here, the radially increasing tangential velocity

of the disk surface creates a pressure gradient, leading to an inflectional radial velocity profile. This system exhibits an inviscid instability, named cross-flow instability, which allows perturbations to grow and form the spiral vortices. These vortices appear co-rotating in their cross sections⁶, and subtend the wave angle ε of around 14° with the outward radial vector.

Since a disk is a cone with half angle $\psi = 90^\circ$, the boundary layer instability mechanism on a rotating broad cone ($30^\circ \lesssim \psi < 90^\circ$) is similar to that over a rotating disk. In still fluid, the cross-flow instability on rotating broad cones leads to the formation of co-rotating spiral vortices^{2,7-14}. When the half-cone angle ψ is decreased from 90° to 15° , the wave angle ε of a vortex, subtended with the meridional line over a rotating cone, decreases from 14° to 0° ^{1,7}. Interestingly, around $\psi = 40^\circ$ to 30° , the instability mechanism changes from the cross-flow to the centrifugal type, due to the dominant effect of centripetal acceleration on the boundary layer for low half cone angles⁷. This results in toroidal vortices over a rotating slender cone ($\psi < 30^\circ$) which are counter-rotating in the cross-section, similar to those observed in concentric cylinders^{15,16}, concave walls¹⁷, and rotating cylinders in cross flow¹⁸⁻²⁰. The exact range of half-cone angles where this change in instability mechanism occurs has not been identified yet. For further discussions, the cones with $\psi \gtrsim 30^\circ$ are considered as broad cones, which are closer to the rotating disk, and the cones with $\psi < 30^\circ$ are considered as slender cones, which are closer to the rotating cylinder case.

When an axial inflow is enforced on rotating cones, both cross-flow and centrifugal instabilities induce spiral vortices. Their onset and growth strongly depend on two parameters: the local Reynolds number $Re_l = \rho u_c l / \mu$ and local rotational speed ratio $S = \omega l / u_c$ ^{21,22}. Here, l is the meridional dis-

This is the author's peer reviewed, accepted manuscript. However, the online version of record will be different from this version once it has been copyedited and typeset.

PLEASE CITE THIS ARTICLE AS DOI: 10.1063/5.0083564

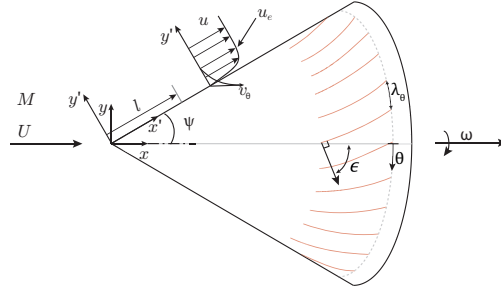


FIG. 1. Schematic of a rotating cone under axial inflow.

tance from the cone apex, ρ is the fluid density, μ is the dynamic viscosity, r is the local radius, ω is the angular velocity of a cone, and u_θ is the velocity just outside the boundary layer^{21–25}. Figure 1 shows a schematic of spiral waves over a rotating cone in axial inflow, along with the geometry parameters.

Although the past literature has explored the boundary-layer instability on rotating cones, the investigations were limited to *low-speed* inflow conditions, i.e. low inflow Reynolds numbers $Re_L = \rho UL/\mu < 10^5$, high base rotational speed ratio $S_b = r_b \omega/U > 1$, and incompressible flow. Here, L is the total meridional length of a cone, r_b is the base radius, ω is the angular velocity and U is the inflow velocity. However, rotating nose-cones of transonic aircraft engines typically face *high-speed* inflow conditions: high inflow Reynolds number $Re_L > 10^6$, low base rotational speed ratio $S_b < 1.5$ and Mach number $M \approx 0.5$ – 0.6 (although the transonic aircraft cruises at Mach number around 0.8, the engine intakes reduce the inflow Mach number for the efficient fan operation^{26,27}). But, the boundary-layer instability on rotating cones remained to be explored in *high-speed* inflow conditions. This hinders in accurately assessing the aerodynamic performance of an aero-engine, and therefore, restricts the design space explorations for any additional efficiency improvements.

Past experiments were limited to the *low-speed* flow regime because they relied on particle-based flow visualisation to detect the instability-induced spiral vortices on rotating cones^{21,28}. They deposited particles (Titanium tetrachloride) on the cone surface before starting an experiment and observed their transport during the operation. Due to several practical challenges, this type of methods are not suitable for *high-speed* experiments, which most-often use blow-down tunnels. For example, due to the short durations (around 20s) of each wind-tunnel run, the cones have to be kept rotating before the wind tunnel starts. For the base rotational speed ratios of interest ($S_b \approx 0.7$ – 1.2), the angular velocity of a cone is high in a *high-speed* inflow, causing high centrifugal forces on the deposited particles on the rotating cone surface. This will cause the particle transfer before the operating conditions are achieved, making the flow visualisation of the instability modes challenging. Recent experimental studies often

use hot-wire anemometry to reconstruct the spiral instability-modes on rotating cones in still fluid^{14,29,30}. However, due to the short operating times of *high-speed* wind-tunnels, scanning the velocity field on rotating cones with a hot-wire probe requires several wind-tunnel runs for each operating point, making it practically infeasible for exploring the parameter space. Therefore, detecting boundary-layer instability on rotating cones remained challenging at flow conditions that are typical for a realistic flight.

In the present work, instead of particle-based visualisation methods and hot-wire anemometry, infrared thermography is used to detect the spiral instability-modes by measuring their thermal footprints on rotating cones in *high-speed* inflow conditions: $Re_L > 10^6$, $S_b < 1$ and $M = 0.5$. The experimental method described in Tambe *et al.*²⁵ is applied here to detect the instability-induced flow features on rotating cones. This method is relatively easy to implement in *high-speed* conditions. It overcomes the limitations of the previously used measurement techniques because the method is non-intrusive and provides instantaneous surface temperature distributions, requiring only a single wind-tunnel run for each operating point. Three different cones with $\psi = 15^\circ$, 30° and 40° are tested. Section II describes the experiments. Section III describes flow fields surrounding the cones in the wind-tunnel test-section. Section IV presents visualisations of the spiral vortices. Section V shows the growth and spatial characteristics of the spiral vortices in the parameter space Re_L vs S_b . Section VI presents observed spiral vortex angles. Section VII concludes the chapter.

II. DESCRIPTION OF EXPERIMENTS

Experiments are performed in TST-27, a transonic-supersonic wind-tunnel at the faculty of Aerospace Engineering, Delft University of Technology (TU Delft). Figure 2 shows a schematic of TST-27. This blow-down wind-tunnel uses pressurised air stored in a separate reservoir at a total pressure between 20 and 40 bar. The pressurised air is expanded through a variable area channel to achieve prescribed flow conditions. A variable choke downstream of the test section is used to achieve a desired subsonic Mach number. The desired Reynolds number is determined by varying the total pressure in the settling chamber. The test-section is rectangular with a constant width of 0.28 m and variable height, which for the present case is 0.253 m. To simulate flow conditions within aero-engines, the wind tunnel is operated at settling chamber pressures between 1.4 and 1.5 bar resulting in $Re_L > 10^6$ and at the inflow Mach number $M = 0.5$. The undisturbed inflow in an empty test section is uniform except the tunnel-wall boundary-layers, as described in appendix A.

Figure 3 shows the measurement setup. As contemporary aero-engines are found to use variety of nose-cone shapes, three different cones are chosen for this investigation: a slender cone with half angle $\psi = 15^\circ$, and two broad cones with $\psi = 30^\circ$ and $\psi = 40^\circ$. Note that previous studies^{7,31} have investigated cones of $\psi = 15^\circ$ and 30° in *low-speed* and therefore, these cases are retained in these *high-speed* investiga-

This is the author's peer reviewed, accepted manuscript. However, the online version of record will be different from this version once it has been copyedited and typeset.

PLEASE CITE THIS ARTICLE AS DOI: 10.1063/1.50083564

3

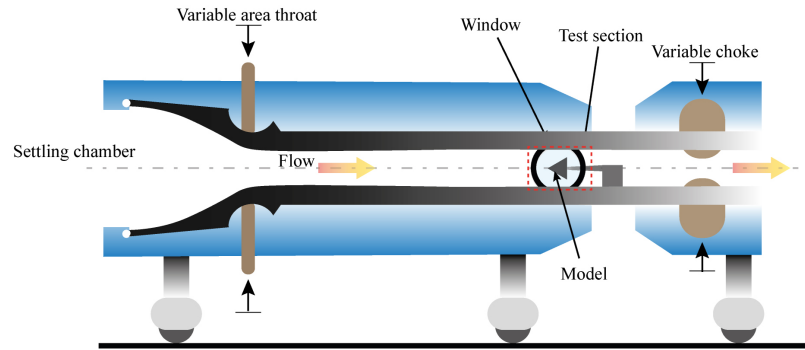


FIG. 2. A schematic of the transonic-supersonic wind-tunnel TST27.

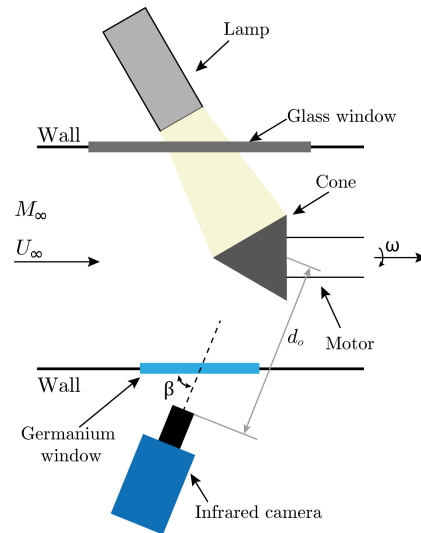


FIG. 3. Measurement setup.

tions. Broader cones with $\psi \gtrsim 45^\circ$ are excluded from the test because they experience high drag which is beyond the limit of the present rotating setup. All the models have a constant base diameter $D = 100$ mm. In the test section, area blockage due to the cone increases from 0% at the tip to 11.1% at the base (excluding the wall boundary-layers), which is comparable to that of a typical aero-engine. The models are rotated by a brushless motor at various rotational speeds (8000 to 36500 RPM) to achieve different combinations of local Reynolds number Re_l and local rotational speed ratio S . The models are made of Polyoxymethylene (POM) which has favourable

thermal properties for the infrared measurements²⁵. The surface is smoothed up to the r.m.s. roughness lower than $1 \mu\text{m}$. The models are statically balanced around the rotation axis. The tip eccentricity is around $5 \mu\text{m}$.

Generally in an unstable system, small environmental disturbances can undergo growth to form coherent flow structures. In the present setup, these disturbances come primarily from three sources: (a) free-stream turbulence of around 3.5–4% of the mean velocity as measured in an empty test section using particle image velocimetry, (b) surface roughness of the cone $\approx 1 \mu\text{m}$ and (c) remnant dust particles in the air below the filter size $< 10 \mu\text{m}$.

Infrared thermography has been shown to be a useful tool for measuring the spiral instability modes over a rotating disk³² and a rotating cone²⁵. This technique is applied in the present study to detect these instability modes from their surface temperature footprints, see figure 3 for the measurement setup. For the half-cone angles $\psi = 40^\circ$, 30° and 15° , the infrared camera has viewing angles $\beta = 71.4^\circ$, 68.7° and 64.9° , and the object distance $d_o = 0.33\text{m}$, 0.4m and 0.47m , respectively. The surface temperature is recorded as the digital pixel intensity I . The integration times of infrared acquisitions are varied between $250\mu\text{s}$ to $25\mu\text{s}$ such that the angle swept by the rotating cones during each acquisition is minimized, while retaining a sufficient signal to noise ratio to measure the surface temperature fluctuations (represented by I'). The results show that at the same operating conditions, different integration times do not significantly alter the observations of instability modes; see appendix B for an example. At high rotation rates (RPM > 30000) of broad cones, the integration times are lowered ($50\mu\text{s}$ to $25\mu\text{s}$), and therefore, the signal contrast is increased by irradiating the cones with a theatre lamp (575W). Table I details the technical specifications of the setup.

Before the wind-tunnel test, both the model and the pressurised stagnant air are at ambient temperature. When the tunnel starts, the air expands into the test-section and the static temperature of the air drops, which cools the model surface. During the wind-tunnel operation time (around 20s),

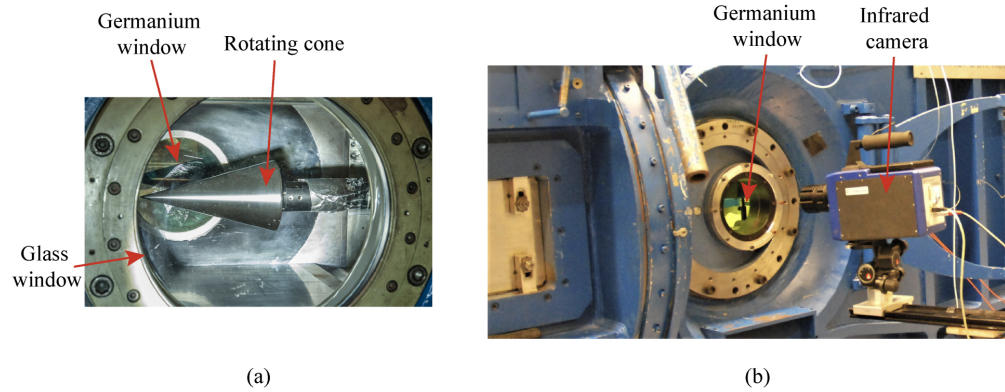


FIG. 4. Photographs showing (a) rotating cone in the test section of TST-27, a transonic-supersonic wind-tunnel and (b) infrared camera viewing through the germanium window.

Camera	FLIR (CEDIP) SC7300 Titanium
Noise equivalent temperature difference (NETD)	25 mK
Spatial resolution	0.43 – 0.6 mm/px
Integration time	25 – 250 μ s
Acquisition frequency	200 Hz
Number of images per dataset	2000
Heat source	Theatre lamp (575 W)

TABLE I. Specifications of the Infrared Thermography setup.

the model cools down and its temperature drops continuously. This trend is removed by subtracting a moving average with the kernel size of 20 instances (corresponding to 0.1s) from the dataset. Since this operation is only a precursor to the subsequent modal analysis, the data after moving mean subtraction is referred to as raw data.

To obtain the local flow properties along the cones, static pressure is measured on the non-rotating cones using a sixteen channel Scanivalve DSA3217 pressure acquisition system. The pressures are measured at different circumferential positions of a cone in a rectangular test-section to obtain a circumferential mean static pressure at a given radius. The total pressure and temperature in the settling chamber, and static pressures at the wind-tunnel walls are also recorded.

III. FLOW FIELD OVERVIEW

The present wind-tunnel configuration features rotating cones in an internal flow, unlike the majority of past studies in low-speed-open-jet facilities. Such internal flow closely represents the most-encountered flow conditions inside an aero-engine. In a symmetry plane, inviscid flow develops between two bounding streamlines near the test-section wall and cone

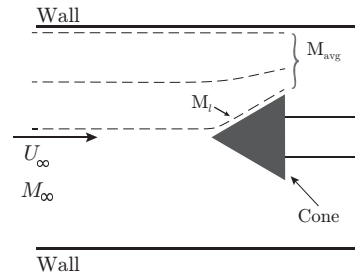


FIG. 5. Schematic of the internal flow within the test section.

surface, see figure 5. Near the cone, the undisturbed oncoming flow slows down upon an encounter with the cone-tip region and turns to follow the cone surface.

Here, estimating flow properties at the edge of a cone boundary-layer is crucial to compute the local flow parameters Re_l and S that govern the stability characteristics over the rotating cones^{21,22}. For this purpose, the local Mach number M_l , just outside the boundary-layer, is obtained us-

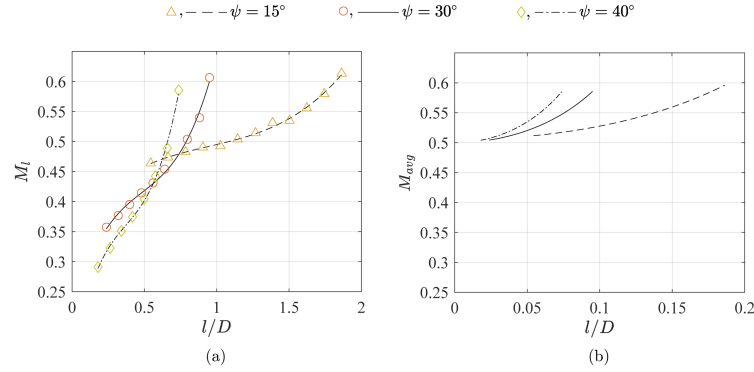


FIG. 6. Mach number variations over the cone meridians: (a) local Mach number of the potential flow near the cone surface obtained from surface pressure measurements and (b) area averaged Mach number of the flow between a cone and test section walls obtained from the local area ratio.

ing the isentropic relations and measured flow properties: circumferential-mean static pressure along the non-rotating cones and total pressure in the settling chamber. This, along with the measured total temperature, gives the local static temperature at the cone surface under the isentropic flow assumption. This gives the local sound speed, which together with the local Mach number M_l is used to calculate the meridional velocity u of an inviscid flow along the cone, with the uncertainty of $\pm 0.038u$. This velocity is used as an approximate estimate of the edge velocity u_e just outside the cone boundary-layer. In *low-speed* studies, this type of assumption is often used where the boundary-layer edge velocity u_e is approximately estimated as the meridional velocity of the potential flow over a cone^{21,23}. Furthermore, local air density is calculated using the ideal-gas relation, and local dynamic viscosity is obtained from the Sutherland's law.

The local Mach number M_l is low near the cone-tip and increases downstream along the cone beyond the free-stream Mach number, see figure 6a. The area-averaged flow Mach number (resulting from one-dimensional-isentropic area-Mach relation) also shows a gradual increase along the cone due to the area contraction, see figure 6b. With increasing half-cone-angle ψ , flow accelerates steeper along the cone, as evident from figure 6.

The local Mach number distributions from figure 6a are used to obtain the flow parameters: local Reynolds number Re_l and rotational speed ratio S . With variable total conditions and rotational speed, different distributions of these parameters are obtained along the cone length to investigate a wider region of the parameter space Re_l vs S .

IV. VISUALISATIONS OF INSTABILITY MODES

The instantaneous surface temperature footprints allow visualising the instability modes over the rotating cones. Proper

orthogonal decomposition (POD) approach is used to identify the modes of surface temperature fluctuations in the measurement dataset, each consisting of 2000 images. The POD modes corresponding to the measurement noise (wavelength $\lambda_\theta < 4$ pixels) are discarded. Remaining POD modes are used to selectively reconstruct the instability modes using criteria based on the azimuthal wavelength λ_θ (see Tambe *et al.*²⁵ for further details).

Figure 7 shows (a) the instantaneous surface temperature fluctuations in the raw data and associated (b and c) POD reconstructions of a rotating broad cone with $\psi = 40^\circ$. The top row images are as observed in the camera sensor plane; and corresponding images in the bottom row are unwrapped cone-surfaces (figures 7d, e and f). The raw data reveal that a wave pattern ($\lambda_\theta \approx \pi r/8$) appears on a rotating cone, overlaid with a long wavelength modulation ($\lambda_\theta > \pi r/4$). These two types of wave patterns are separated using POD modes. The long wavelength modulation is reconstructed using the POD modes having an azimuthal wavelength $\lambda_\theta > \pi r/4$, i.e. an azimuthal number of waves $n < 8$, see figures 7b and e. The short-wavelength pattern is reconstructed from the POD modes having an azimuthal wavelength between $\pi r/4 > \lambda_\theta > 4$ pixels, see figures 7c and f; this pattern shows nearly constant azimuthal spacing, which indicates azimuthal coherence.

Similar short and long wave temperature patterns have been observed on rotating cones in *low-speed* conditions (e.g., see Tambe *et al.*²⁵). The *low-speed* investigations have clarified that the short-wave temperature pattern corresponds to the spiral vortices, and the long-wave pattern is aligned with the spiral vortices. This can be viewed as the azimuthal modulation of the spiral vortex strength. The striking similarity of the patterns observed in *low-speed* and present *high-speed* case suggests that the short-wave pattern in figure 7c corresponds to the footprint of the spiral vortices. Further investigation is required to identify the physical reasoning behind the appearance of the long-wave pattern.

Similar wave patterns are observed also for a rotating broad cone with $\psi = 30^\circ$, as shown in figure 8. Here, a coherent spiral vortex footprints with $\lambda_\theta \approx \pi r/5$ (figures 8c and f) has a major contribution to the raw image (figures 8a and d), in addition to the long wave modulation (figures 8b and e).

The stability analyses of rotating broad cones in compressible still fluid¹² and with incompressible axial inflow⁸ have shown that, with decreasing half-cone angle ψ , the range of unstable wavelengths gets broadened, and increasingly longer wavelengths can destabilise the flow. Results of Kobayashi and Izumi⁷ agree with this trend as the azimuthal number decreases (wavelength increases) with decreasing half-cone angle ψ . A similar trend is observed in the present study, where, for a lower half cone angle $\psi = 30^\circ$ (figure 8), longer wavelengths of $\lambda_\theta \approx \pi r/5$ are observed as compared to $\lambda_\theta \approx \pi r/8$ observed for $\psi = 40^\circ$ (figure 7).

Figure 9 shows a raw image and the corresponding POD reconstructions for a slender cone with $\psi = 15^\circ$. Here, a coherent spiral vortex pattern of $\lambda_\theta \approx \pi r/4$ (figure 9c) is observed along with the long wave modulation (figure 9b). However, on the slender cone, other instances with coherent patterns of $\lambda_\theta \lesssim \pi r/3$ are also observed, see figure 17 for example. Therefore, the upper bound for the low-order reconstructions in figures 9c and f is set at $\pi r/3$ (relating to the azimuthal number $n = 6$) instead of $\pi r/4$ (relating to the azimuthal number $n = 8$) used for broad cones. This highlights the need of a separate investigation to identify these vortices by measuring the velocity field.

Overall, the visualizations show that, in *high-speed* conditions of $M = 0.5$ and $Re_L > 10^6$, the instability modes over rotating cones appear to be spiral vortices, similar to those observed in *low-speed* conditions. The spiral vortex patterns on broad cones (figures 7 and 8) are similar to the spiral vortices observed in the *low-speed* cases over rotating disks and broad cones; compare figures 7 and 8 with visualisations of Kobayashi¹, Kohama^{2,6}. On a rotating slender cone, the spiral vortex fronts are oriented more towards the axial direction as compared to the past *low-speed* studies^{21,25}. This is expected as the present observations on slender cones are at low local rotational speed ratios $S < 0.5$, whereas past *low-speed* studies encountered high rotational speed ratio $S > 1$. This agrees with the previously identified trend where with decreasing rotational speed ratio spiral vortex-fronts become more axial.

Flow investigations in a meridional plane are necessary to confirm whether these spiral vortices are co- or counter-rotating. Due to the limitations of the present experiments, i.e. limited optical access for a PIV light-sheet, the cross-sections of the spiral vortices in the meridional plane remains unknown.

V. GROWTH OF SPIRAL VORTICES

The spiral vortices observed in the present study are convective instability modes. The effect of their spatial growth on the surface temperature fluctuations is observed from the statistical RMS of the thermal footprints I'_{RMS} on a rotating cone,

computed over a dataset (2000 images, acquired at 200Hz). Figure 10a shows I'_{RMS} on a rotating broad cone ($\psi = 30^\circ$), computed over a raw dataset containing the instance shown in figure 8a. The region where the spiral vortices appear shows high levels of temperature fluctuations. The RMS fluctuations are axisymmetric because of the symmetry of axial inflow. Therefore, the spatial growth of the spiral vortices is characterised using a circumferential mean of I'_{RMS} along the meridional lines (see figure 10b). Downstream from the cone apex ($l/D = 0$), the I'_{RMS} stays low until a point ($l/D \approx 0.57$) where it suddenly starts growing. This location relates to a critical point suggesting the onset of the spiral vortex growth. At their origin, the spiral vortices are expected to have weak thermal footprints which is usually below the measurement sensitivity³¹. Therefore, a critical point in the present case relates to the onset of a rapid growth of the spiral vortices rather than the point of their origin. This point is objectively defined as an intersection of the linear parts of I'_{RMS} curve (approximated with least square linear fits shown as gray lines in 10b). The growth of the spiral vortices continues until a maximum amplification ($l/D \approx 0.72$), after which I'_{RMS} starts to decrease.

In figure 11, the curves of Re_l vs S show how these flow parameters vary over a cone at different operating conditions. The critical and maximum amplification points on these curves mark the region of the spiral vortex growth. The Reynolds numbers corresponding to these points decrease with the rotational speed ratio S . With increasing half-cone angle ψ and for a fixed Reynolds number Re_l , critical and maximum amplification points of the spiral vortex growth appear to shift towards higher rotational speed ratios S . This suggests that with increasing half-cone angle the boundary-layer becomes more stable such that a stronger relative rotation effect (represented by higher rotational speed ratio S) is required to cause the spiral vortex growth. Previously, this trend has been observed for rotating cones in still fluid⁷ and predicted for rotating broad cones in incompressible axial inflow²². However, understanding the mechanism behind this trend requires a separate theoretical analysis, which is beyond the scope of the present work.

Figure 12 compares the spiral vortex growth region at the present *high-speed* conditions with the *low-speed* investigations from the literature. Kobayashi *et al.*²³ have tested rotating cones with varying free-stream turbulence level in *low-speed* conditions. Their observations show that the transition Reynolds number, where the velocity fluctuations start to resemble a typical turbulent spectrum, remains unaltered by the free-stream turbulence level. However, the critical Reynolds number (corresponding to the onset of instability modes) is lowered by a higher intensity of the free-stream turbulence (see figure 12). Consequently, the region between the critical and transition points (transition region) becomes broader. The free-stream turbulence level in the present experiments is around 3.5 – 4% of the free-stream velocity U . Therefore, the present study can be compared to the *low-speed* results of Kobayashi *et al.*²³ with the similar turbulence intensity (3.6% of U). The comparison suggests that the transition region (as schematically highlighted in figure 12) reported in past *low-*

This is the author's peer reviewed, accepted manuscript. However, the online version of record will be different from this version once it has been copyedited and typeset.

PLEASE CITE THIS ARTICLE AS DOI: 10.1063/1.50083564

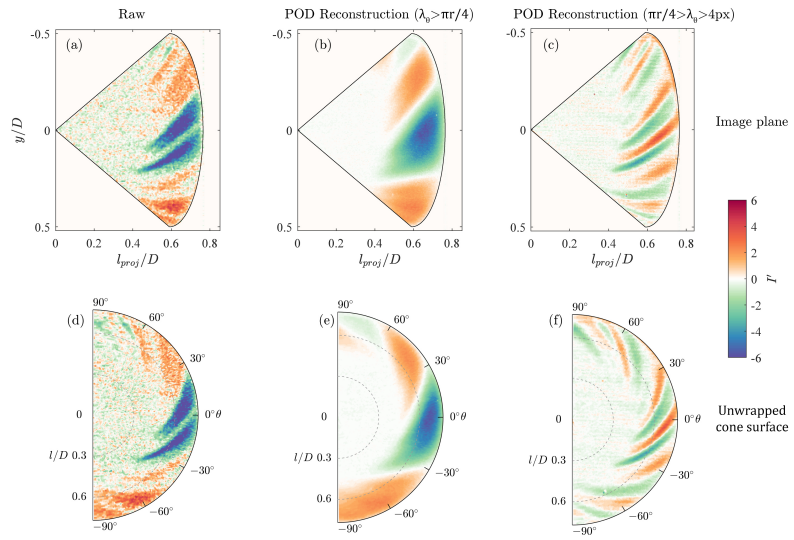


FIG. 7. Thermal footprints of the spiral instability modes and their POD reconstructions over a rotating broad cone with half angle $\psi = 40^\circ$ shown in image planes (top row) as well as unwrapped cone surfaces (bottom row). (a) and (d) raw instance, (b) and (e) POD reconstruction of a long-wave pattern ($\lambda_\theta > \pi r/4$), (c) and (f) POD reconstruction of a short-wave pattern ($\pi r/4 > \lambda_\theta > 4px$). $Re_L = 1.3 \times 10^6$ and $S_b = 1.1$.

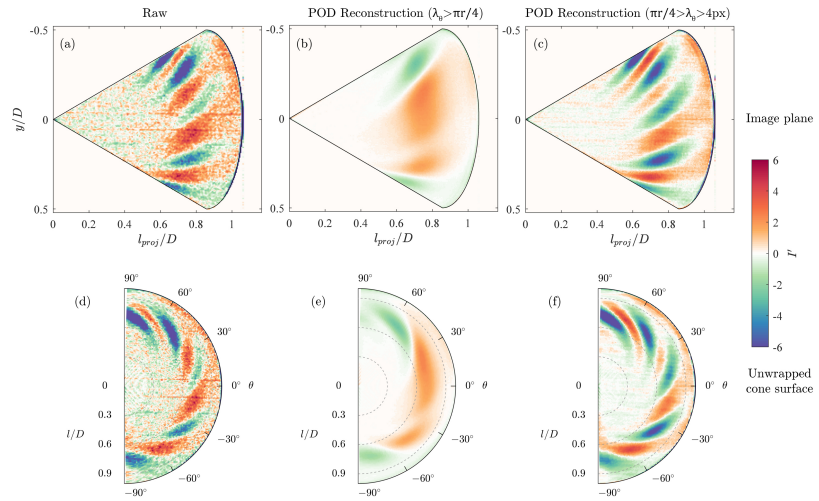


FIG. 8. Thermal footprints of the spiral instability modes and their POD reconstructions over a rotating broad cone with half angle $\psi = 30^\circ$ shown in image planes (top row) as well as unwrapped cone surfaces (bottom row). (a) and (d) raw instance, (b) and (e) POD reconstruction of a long-wave pattern ($\lambda_\theta > \pi r/4$), (c) and (f) POD reconstruction of a short-wave pattern ($\pi r/4 > \lambda_\theta > 4px$). $Re_L = 1.4 \times 10^6$ and $S_b = 1$.

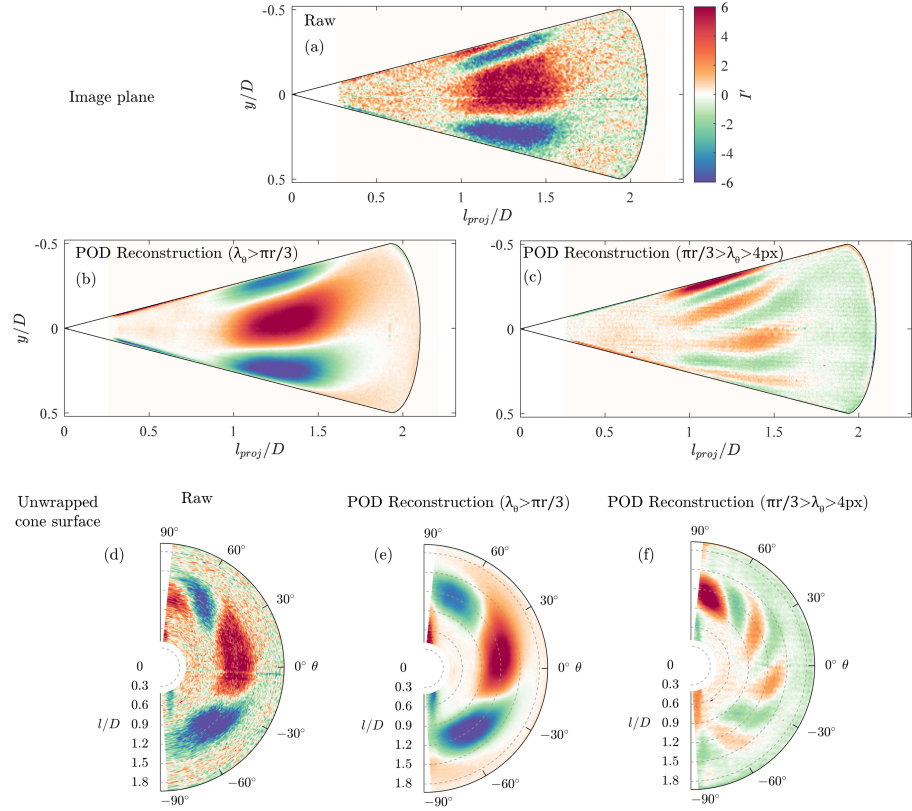


FIG. 9. Thermal footprints of the spiral instability modes and their POD reconstructions over a rotating slender cone with half angle $\psi = 15^\circ$ shown in image planes (top rows) as well as unwrapped cone surfaces (bottom row). (a) and (d) raw instance, (b) and (e) POD reconstruction of a long-wave pattern ($\lambda_\theta > \pi r/3$), (c) and (f) POD reconstruction of a short-wave pattern ($\pi r/3 > \lambda_\theta > 4px$). $Re_L = 3.2 \times 10^6$ and $S_b = 0.72$.

speed studies, can be extrapolated to the *high-speed* conditions of the present study. This shows that the spiral instability modes similar to those studied in the past can be expected on real aero-engine nose-cones.

Figure 13 shows the maximum amplification points on rotating cones in *low-* and *high-speed* inflows; obtained from the literature (available only for $\psi = 15^\circ$)³¹ and present investigation, respectively. For the investigated cones of $\psi = 15^\circ$, the instability behaviour remains the same in *low-* and *high-speed* cases. Here, maximum amplification Reynolds number follows an exponential relation with the rotational speed ratio $Re_{L,m} = CS^{a_1}$, extending from *low-speed* to *high-speed* conditions (shown using dashed line in figure 13). Here, constants C and a_1 are expected to depend on half-cone angle ψ . For $\psi = 15^\circ$, $a_1 = -2.62$ and $C = 2.3 \times 10^5$. The present *high-speed* investigation is performed in a close-test section where

the area contraction accelerates the flow along the cone, unlike in the *low-speed* investigations in an open-jet. However, this does not seem to affect the maximum amplification of the spiral vortices in Re_l vs S space (figure 13). Moreover, increasing inflow Mach number from $M < 0.02$ to $M = 0.5$ has insignificant effect on the trend of maximum amplification points in Re_l vs S space (for $\psi = 15^\circ$).

VI. SPIRAL VORTEX ANGLE

The spiral vortex angle ε is obtained from the POD reconstructions as shown in figure 14. Here, the spiral vortices appear linear in l, θ coordinate system. First, a trace of temperature fluctuations (T') over a 60° sector is obtained along θ , at a fixed l/D . This trace is cross-correlated with tem-

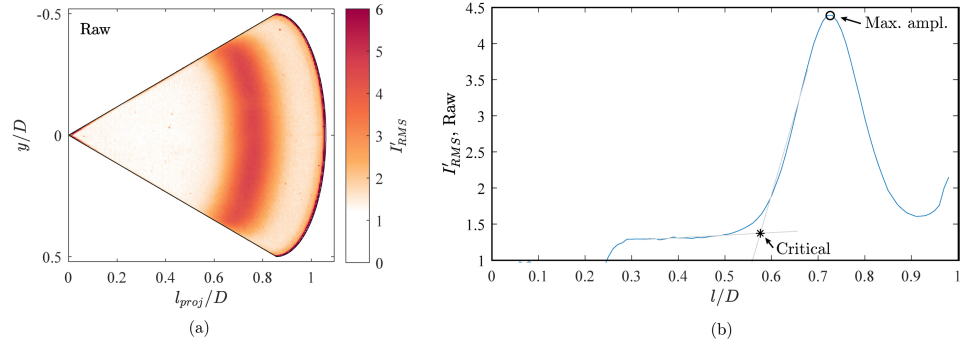


FIG. 10. RMS of surface temperature fluctuations in a dataset over a rotating broad cone ($\psi = 30^\circ$) shown in an (a) image plane and (b) a circumferential average along the meridional length for raw data. $Re_L = 1.4 \times 10^6$ and $S_b = 1$.

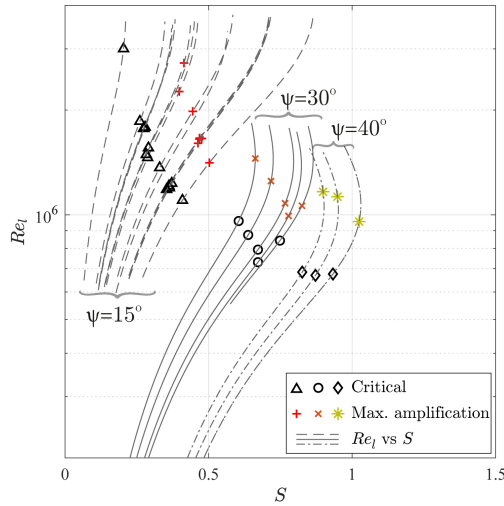


FIG. 11. Growth characteristics of the spiral vortices.

perature fluctuation patterns at an incremented l/D , sliding along the whole range of θ and a cross-correlation peak is found. This procedure is repeated on the new peak location until the whole transition region is scanned. A least-square linear curve (shown as red in figure 14a) is fitted to the loci of cross-correlation peaks (shown as circles in figure 14a) : $\theta = ml + c$ (where m and c are fit parameters). The spiral vortex angle is obtained as $\varepsilon = \sin^{-1}(1/\sqrt{1+l^2m^2\sin^4(\psi)})$.

As from *low-speed* studies, the spiral vortex angle depends on the local rotational speed ratio S^{21} . Generally, the spiral vortex angle increases with decreasing rotational speed

ratio S . Physically, this means that as the effect of rotation is reduced, the spiral vortex fronts turn towards the oncoming flow direction. A similar trend is observed at *high-speed* conditions, as evident from comparing present spiral vortex angles with the *low-speed* data from Kobayashi *et al.*²³ in figure 15. In this case, the measured spiral vortex angles in *high-speed* cases agree well with those from the *low-speed* studies. This suggests that the Reynolds number does not influence the spiral vortex angles. Figure 15b is a zoomed in view of figure 15, showing the measured spiral vortex angle ε .

VII. CONCLUSION

The instability of the boundary-layers over rotating cones is studied in an enforced *high-speed* flow at $Re_L > 10^6$ and $M = 0.5$. Two broad cones with half angles $\psi = 30^\circ$ and 40° and a slender cone with $\psi = 15^\circ$ are tested in a transonic-supersonic wind tunnel. The instability modes are identified from their surface temperature footprints, measured using infrared thermography. Following are the important conclusions:

1. Visualisations show that instability induced spiral vortices appear on rotating cones facing *high-speed* inflow at $Re_L > 10^6$ and $M = 0.5$, similar to the inflows in aero-engines. Their appearance is similar to the spiral vortices observed over rotating cones in *low-speed* conditions.
2. In *high-speed* conditions, the surface temperature on rotating cones fluctuates in two distinct patterns: a short wavelength footprints of spiral vortices and long wavelength modulations of the spiral vortex strength. These patterns show similarities with those observed in the *low-speed* cases.
3. Local Reynolds number Re_l and rotational speed ratio S govern the growth of spiral vortices as expected from

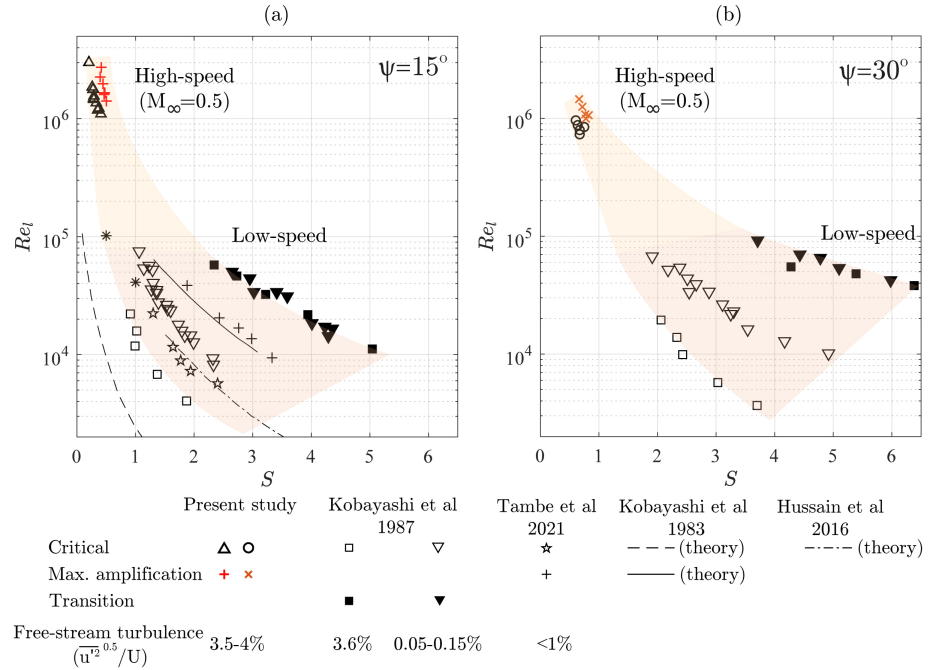


FIG. 12. Comparisons of the growth characteristics of the spiral vortices at *high-speed* conditions to those reported in the literature for *low-speed* conditions^{21,23,24,31}. (a) $\psi = 15^\circ$ and (b) $\psi = 30^\circ$.

low-speed studies.

- At a fixed local Reynolds number Re_l , increasing half-cone angle ψ shifts the growth of the spiral vortices at higher rotational speed ratios S . This trend was also observed in past *low-speed* studies.
- The maximum amplification Reynolds number follows an exponential relation with the rotational speed ratio $Re_{l,m} = CS^{a_1}$, extending from *low-* to *high-speed* conditions. Constants C and a_1 are expected to depend on the half-cone angle ψ . For $\psi = 15^\circ$, $a_1 = -2.62$ and $C = 2.3 \times 10^5$.
- The trend of spiral vortex angle ε variation w.r.t. the rotational speed ratio S is common in both *low-* and *high-speed* conditions.

This study has experimentally explored the parameter space of boundary-layer instability on rotating cones to the flow conditions relevant to aerospace applications, e.g. aero-engine-nose-cones during a transonic flight. The study has shown that the instability-induced spiral vortices can be expected to appear on nose-cones of civil transport aircraft. This is evidently observed as the boundary-layer transition region on

rotating cones extends to the parameter space of Re_l vs S at $Re_l > 10^6$ and $S \lesssim 1$ in a similar fashion as expected from the past *low-speed* studies. Comparison of *low-* and *high-speed* investigations shows that the local flow Mach number $M_l = 0.02$ - 0.6 does not influence the maximum amplification points in the Re_l vs S space. However, the cross-sectional view of the spiral vortices remains to be investigated. This information can help in identifying the underlying instability mechanism, as centrifugal instability induces counter-rotating vortices and cross-flow instability usually induces co-rotating vortices¹. Furthermore, the effect of surface roughness on the spiral vortex growth needs to be investigated, as in reality, aero-engine nose cones may experience surface roughness as isolated elements from foreign object impacts, or as distributed roughness arising from, fasteners, manufacturing and coating techniques.

ACKNOWLEDGEMENT

The authors thank technical staff—Peter Duyndam, ir. Frits Donker Duyvis, ir. Eric de Keizer, Dennis Bruikman, and Henk-Jan Siemer—of High-speed lab, AWE, Aerospace Engineering, TU Delft for their technical support during the ex-

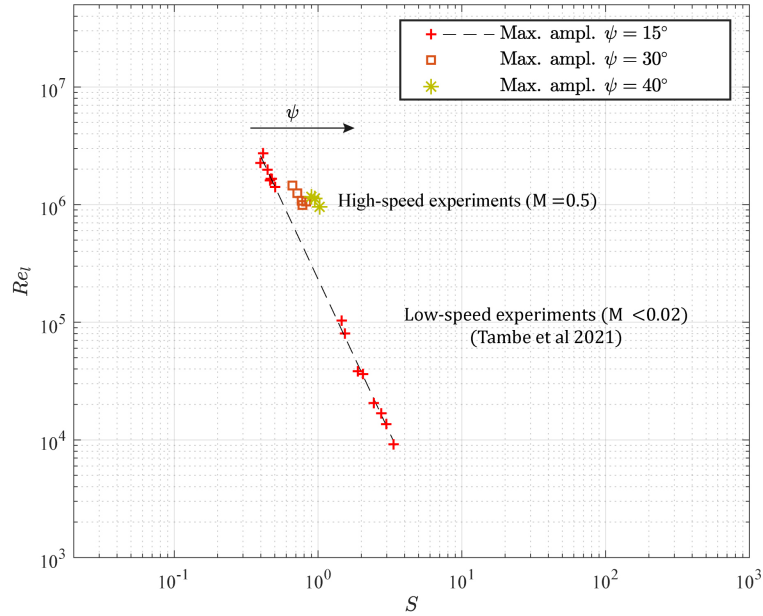


FIG. 13. Maximum amplification points of the spiral vortex growth on rotating cones in present *high-speed* cases compared to the *low-speed* case³¹.

periments. This work was funded by the European Union Horizon 2020 program: Clean Sky 2 Large Passenger Aircraft (CS2-LPA-GAM-2018-2019-01), and CENTRELINE (Grant Agreement No. 723242).

CONFLICT OF INTEREST

Authors have no conflict of interest to report.

Appendix A: Undisturbed inflow

The inflow velocity is measured using two-component planar particle image velocimetry (PIV) in a symmetry plane of the empty test section (without a model). The image pairs are captured using LaVision imager sCMOS camera equipped with 105mm Nikkor objective lens. The flow is seeded with DEHS droplets of size $\approx 1\mu\text{m}$. The particles are illuminated with double-pulsed laser Evergreen 200. Commercial software DaVis 8.4.0 is used for image acquisition and vector calculations. A multipass approach with decreasing interrogation window size (from 128×128 pixels to 32×32 pixels) is used to compute the vectors resulting in a vector pitch of 0.23mm. The total of 450 image pairs are acquired at the rate of 10Hz (using three windtunnel runs of 150 image pairs each).

The velocity measurements show that the undisturbed inflow in an empty test section of TST27 windtunnel is uniform, as seen from the time-averaged stream-wise velocity (u) in figure 16a. It is known from the previous boundary-layer studies performed in this windtunnel (although supersonic, but at the order of Reynolds number comparable with the present study), that the order of displacement thickness of the tunnel wall boundary-layers is usually below 1% of the test section width (also, $\delta_{99} < 7\%$ of the test section width)³³. Therefore, this does not pose any non-uniformity to the cones placed at the centre of the test-section because their base diameter is only around 35% of the test section width. Figure 16b shows the typical turbulence intensity distribution of the inflow in terms of RMS of streamwise velocity fluctuations u'_{RMS} .

Appendix B: Effect of integration time

In the present study, the cones are rotated at high r.p.m. (8000 to 33000) to achieve the desired rotational speed ratios in *high-speed* inflow. Spiral vortices are observed with an infrared camera at finite integration times, ranging from $25\mu\text{s}$ to $205\mu\text{s}$. During the integration time, a cone surface rotates with respect to a stationary camera sensor plane. A sensor records the temperature of this moving surface as it passes through its field of view. For a coherent spiral vortex pattern

This is the author's peer reviewed, accepted manuscript. However, the online version of record will be different from this version once it has been copyedited and typeset.

PLEASE CITE THIS ARTICLE AS DOI: 10.1063/1.50083564

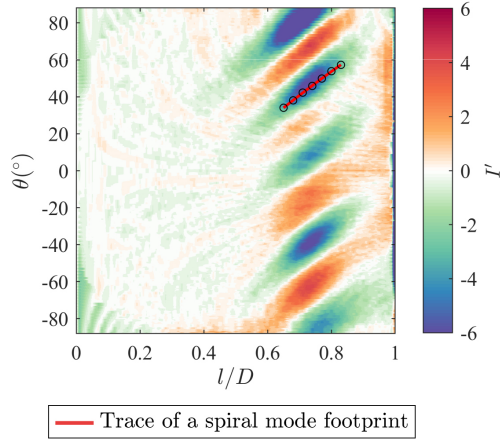


FIG. 14. Traced wavefront of the spiral modes in l and θ space used to obtain the wave angle ε .

this does not alter the observed pattern. Figure 17 shows the rotating cone at same operating conditions but observed with three integration times $t_{int} = 205\mu s$, $105\mu s$ and $50\mu s$. The long wave modulations do not show any significant difference, see figures 17b, e and h. The short wavelength patterns get slightly sharper with decreasing integration time, see figures 17c, f and i.

The locations where the spiral vortex growth is observed does not show significant changes with changing integration time, see figure 18a. As expected, the lower integration time reduces the signal strength as evident from the reduced I'_{RMS} at $t_{int} = 50\mu s$ as compared to that at $t_{int} = 205\mu s$ in figure 18. The effect of integration time on the spiral vortex angle ε is also minimal, as evident from figure 18b.

AIP PUBLISHING DATA SHARING POLICY

The data that support the findings of this study are available from the corresponding author upon reasonable request.

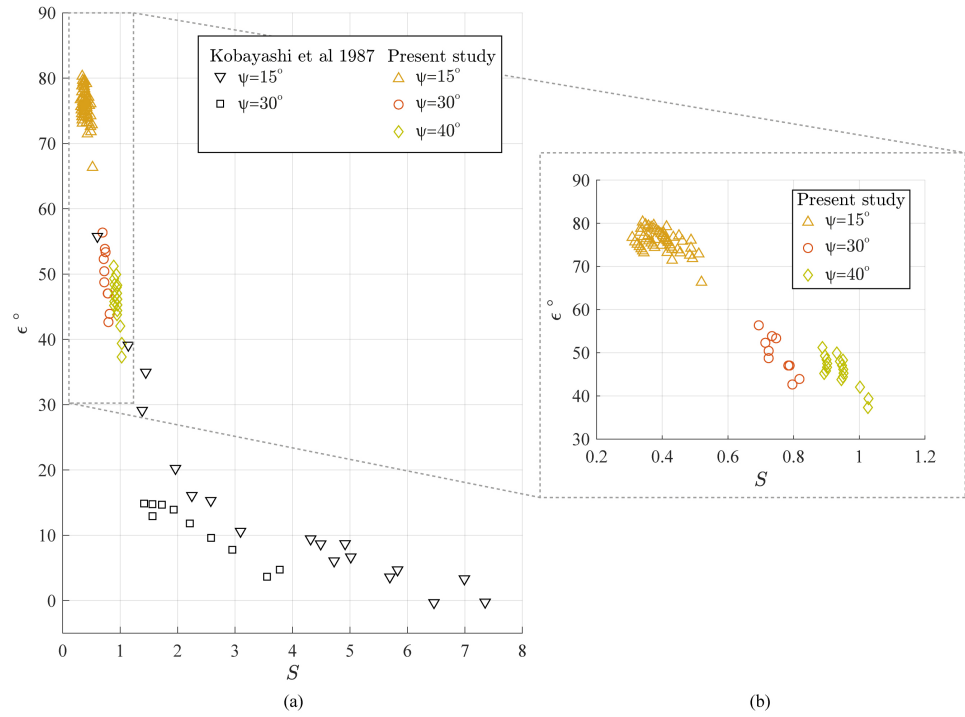


FIG. 15. (a) Comparisons of the wave angle ϵ obtained in the present study to those reported in the literature²¹ against the local rotational speed ratio S . (b) A zoomed-in view of the vortex angles obtained in the present study.

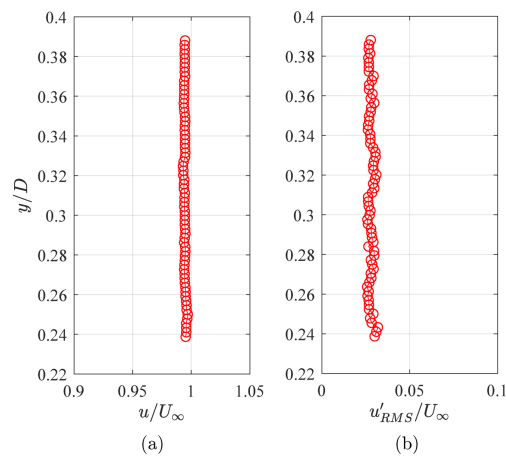


FIG. 16. Undisturbed inflow profiles in an empty test section (a) time-averaged stream-wise velocity and (b) turbulence intensity.

This is the author's peer reviewed, accepted manuscript. However, the online version of record will be different from this version once it has been copyedited and typeset.

PLEASE CITE THIS ARTICLE AS DOI: 10.1063/5.0083564

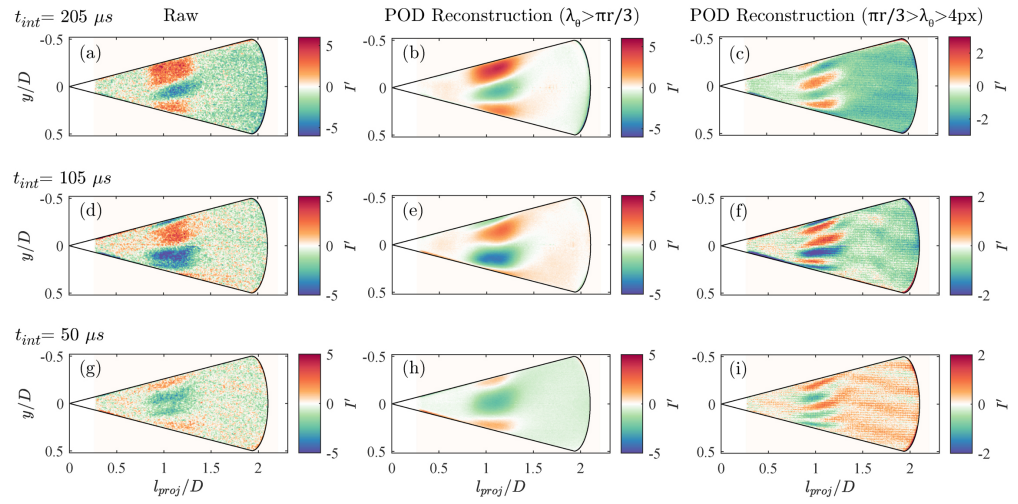


FIG. 17. Effect of integration time t_{int} on the thermal footprint measurements of the spiral vortices. (a),(d),(g) raw instance, (b),(e),(h) POD reconstruction of a long-wave pattern ($\lambda_\theta > \pi r/3$), and (c),(f),(i) POD reconstruction of a short-wave pattern ($\pi r/3 > \lambda_\theta > 4px$). (a),(b),(c) $t_{int} = 205\mu s$, (d),(e),(f) $t_{int} = 105\mu s$, (g),(h),(i) $t_{int} = 50\mu s$.

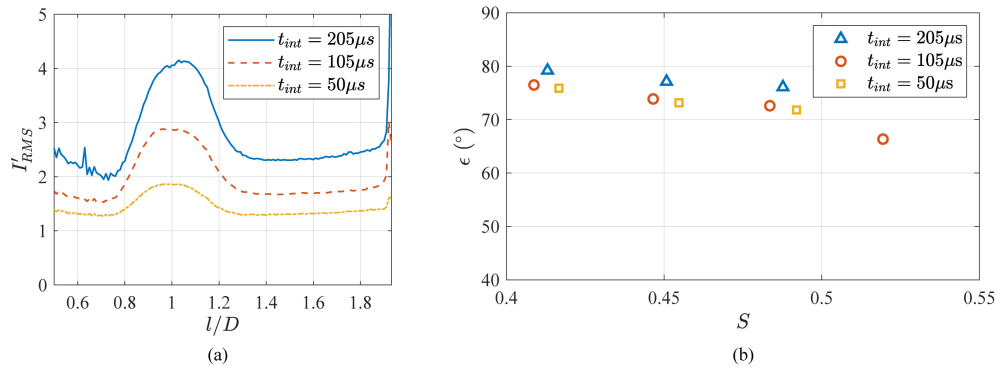


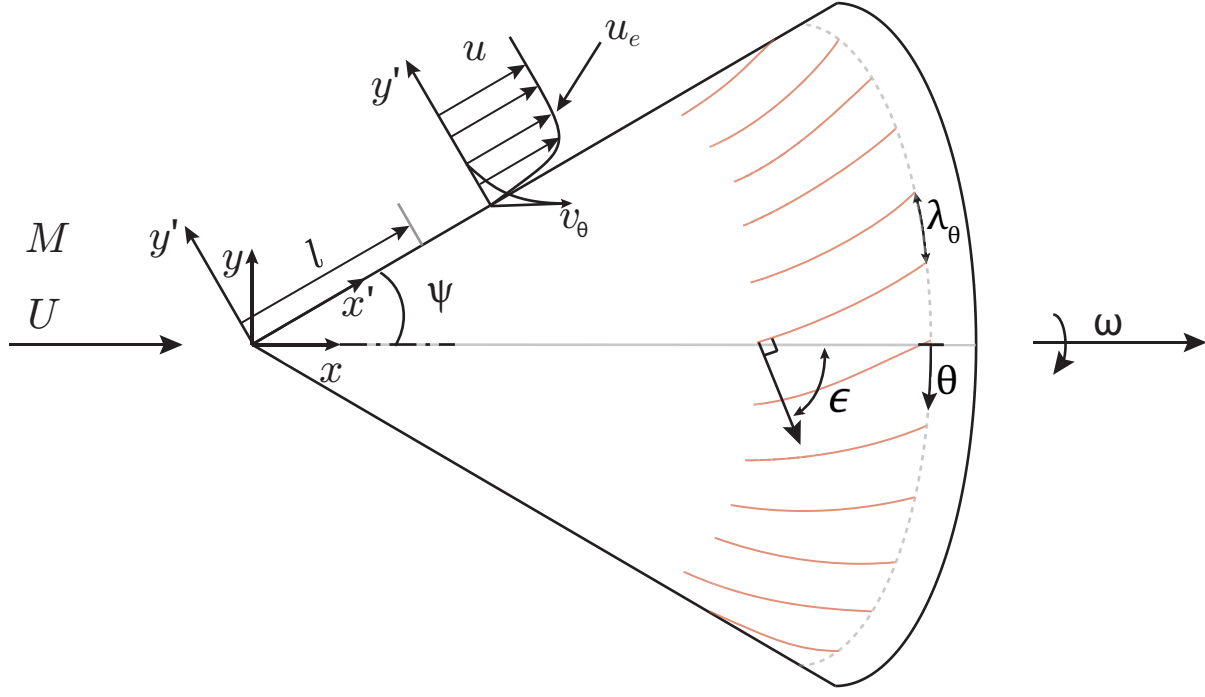
FIG. 18. Effect of integration time t_{int} on (a) surface temperature fluctuations I'_{RMS} and (b) spiral vortex angle ϵ .

This is the author's peer reviewed, accepted manuscript. However, the online version of record will be different from this version once it has been copyedited and typeset.

PLEASE CITE THIS ARTICLE AS DOI: 10.1063/5.0083564

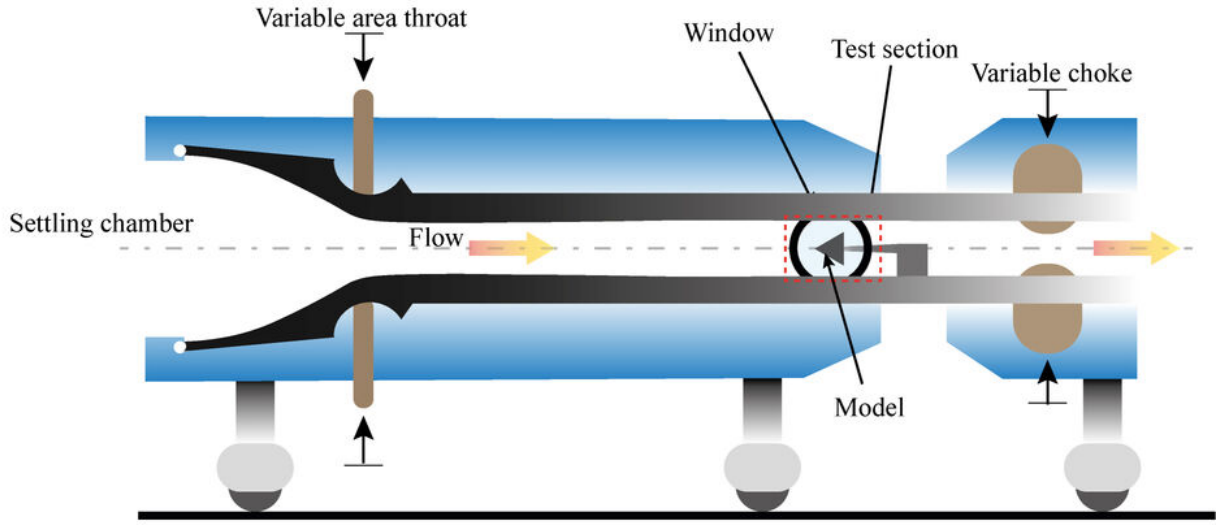
- ¹R. Kobayashi, "Review: laminar-to-turbulent transition of three-dimensional boundary layers on rotating bodies," *Journal of fluids engineering* **116**, 200–211 (1994).
- ²Y. P. Kohama, "Three-dimensional boundary layer transition study," *Current Science* **79**, 800–807 (2000).
- ³A. D. Scillitoe, P. G. Tucker, and P. Adami, "Numerical investigation of three-dimensional separation in an axial flow compressor: The influence of freestream turbulence intensity and endwall boundary layer state," *Journal of Turbomachinery* **139**, 1–10 (2017).
- ⁴N. H. Smith, "Exploratory investigation of laminar-boundary-layer oscillations on a rotating disk," Tech. Rep. 1227 (1947).
- ⁵B. Y. N. Gregory, J. T. Stuart, and W. S. Walker, "On the Stability of Three-Dimensional Boundary Layers with Application to the Flow Due to a Rotating Disk," *Philosophical Transactions of the Royal Society of London. Series A, Mathematical and Physical Sciences* **248**, 155–199 (1955).
- ⁶Y. Kohama, "Study on boundary layer transition of a rotating disk," *Acta Mech.* **50**, 193–199 (1984).
- ⁷R. Kobayashi and H. Izumi, "Boundary-layer transition on a rotating cone in still fluid," *Journal of Fluid Mechanics* **127**, 353–364 (1983).
- ⁸S. J. Garrett, Z. Hussain, and S. O. Stephen, "The cross-flow instability of the boundary layer on a rotating cone," *Journal of Fluid Mechanics* **622**, 209–232 (2009).
- ⁹P. D. Towers and S. J. Garrett, "On the stability of the compressible boundary-layer flow over a rotating cone," 42nd AIAA Fluid Dynamics Conference and Exhibit 2012 **44**, 1–9 (2012).
- ¹⁰P. D. Towers, *The stability and transition of the compressible boundary-layer flow over broad rotating cones*, Ph.D. thesis, University of Leicester (2013).
- ¹¹P. D. Towers and S. J. Garrett, "Similarity solutions of compressible flow over a rotating cone with surface suction," *Thermal Science* **20**, 517–528 (2016).
- ¹²P. D. Towers, Z. Hussain, P. T. Griffiths, and S. J. Garrett, "Viscous modes within the compressible boundary-layer flow due to a broad rotating cone," *IMA Journal of Applied Mathematics (Institute of Mathematics and Its Applications)* **81**, 940–960 (2016).
- ¹³K. Kato, P. H. Alfredsson, and R. J. Lingwood, "Boundary-layer transition over a rotating broad cone," *Physical Review Fluids* **4**, 71902 (2019).
- ¹⁴K. Kato, T. Kawata, P. H. Alfredsson, and R. J. Lingwood, "Investigation of the structures in the unstable rotating-cone boundary layer," *Physical Review Fluids* **4**, 1–30 (2019).
- ¹⁵G. I. Taylor, "Stability of Viscous Liquid contained between Two Rotating Cylinders," *Philosophical Transactions of the Royal Society of London. Series A, Containing Papers of a Mathematical or Physical Character* **223**, 289–343 (1923).
- ¹⁶P. G. Drazin, *Introduction to Hydrodynamic Stability* (Cambridge University Press, 2002).
- ¹⁷H. Görtler, "On the Three-Dimensional Instability of Laminar Boundary Layers on Concave Walls," Tech. Rep. (NACA, 1954).
- ¹⁸S. Mittal, "Three-dimensional instabilities in flow past a rotating cylinder," *Journal of Applied Mechanics, Transactions of the ASME* **71**, 89–95 (2004).
- ¹⁹A. Radi, M. C. Thompson, A. Rao, K. Hourigan, and J. Sheridan, "Experimental evidence of new three-dimensional modes in the wake of a rotating cylinder," *Journal of Fluid Mechanics* **734**, 567–594 (2013).
- ²⁰A. Rao, J. Leontini, M. C. Thompson, and K. Hourigan, "Three-dimensionality in the wake of a rotating cylinder in a uniform flow," *Journal of Fluid Mechanics* **717**, 1–29 (2013).
- ²¹R. Kobayashi, Y. Kohama, and M. Kurosawa, "Boundary-layer transition on a rotating cone in axial flow," *Journal of Fluid Mechanics* **127**, 353–364 (1983).
- ²²S. J. Garrett, Z. Hussain, and S. O. Stephen, "Boundary-Layer Transition on Broad Cones Rotating in an Imposed Axial Flow," *AIAA Journal* **48**, 1184–1194 (2010).
- ²³R. Kobayashi, Y. Kohama, T. Arai, and M. Ukaku, "The Boundary-layer Transition on Rotating Cones in Axial Flow with Free-stream Turbulence," *JSME International Journal* **30**, 423–429 (1987).
- ²⁴Z. Hussain, S. J. Garrett, S. O. Stephen, and P. T. Griffiths, "The centrifugal instability of the boundary-layer flow over a slender rotating cone in an enforced axial free stream," *Journal of Fluid Mechanics* **788**, 70–94 (2016).
- ²⁵S. Tambe, F. Schrijer, A. G. Rao, and L. Veldhuis, "An experimental method to investigate coherent spiral vortices in the boundary layer over rotating bodies of revolution," *Experiments in Fluids* **60**, 115 (2019).
- ²⁶A. Peters, Z. S. Spakovszky, W. K. Lord, and B. Rose, "Ultrashort nacelles for low fan pressure ratio propulsors," *Journal of Turbomachinery* **137** (2015), 10.1115/1.4028235.
- ²⁷K. Uenishi, M. S. Pearson, T. R. Lehnig, and R. M. Leon, "CFD-based 3D turdofan nacelle design system," in *AIAA 8th Applied Aerodynamics Conference* (1990) pp. 1–18.
- ²⁸Y. Kohama, "Behaviour of spiral vortices on a rotating cone in axial flow," *Acta Mechanica* **51**, 105–117 (1984).
- ²⁹K. Kato, A. Segalini, P. H. Alfredsson, and R. J. Lingwood, "Instabilities and transition on a rotating cone—old problems and new challenges," in *IUTAM Laminar-Turbulent Transition*, edited by S. Sherwin, P. Schmid, and X. Wu (Springer International Publishing, Cham, 2022) pp. 203–213.
- ³⁰K. Kato, A. Segalini, P. H. Alfredsson, and R. J. Lingwood, "Instability and transition in the boundary layer driven by a rotating slender cone," *Journal of Fluid Mechanics* **915**, 1–11 (2021).
- ³¹S. Tambe, F. Schrijer, A. G. Rao, and L. Veldhuis, "Boundary layer instability over a rotating slender cone under non-axial inflow," *Journal of Fluid Mechanics* **910** (2021).
- ³²T. Astarita, G. Cardone, G. M. Carlomagno, and P. Tecchio, "Spiral Vortices Detection on a Rotating Disk," in *ICAS 2002 CONGRESS* (2002) pp. 1–8.
- ³³R. Giepmans, A. Srivastava, F. Schrijer, and B. van Oudheusden, "The effects of Mach and Reynolds number on the flow mixing properties of micro-ramp vortex generators in a supersonic boundary layer," in *45th AIAA Fluid Dynamics Conference*, June (2015) pp. 1–19.

This is the author's peer reviewed, accepted manuscript. However, the online version of record will be different from this version once it has been copyedited and typeset.
 PLEASE CITE THIS ARTICLE AS DOI: 10.1063/1.50083564



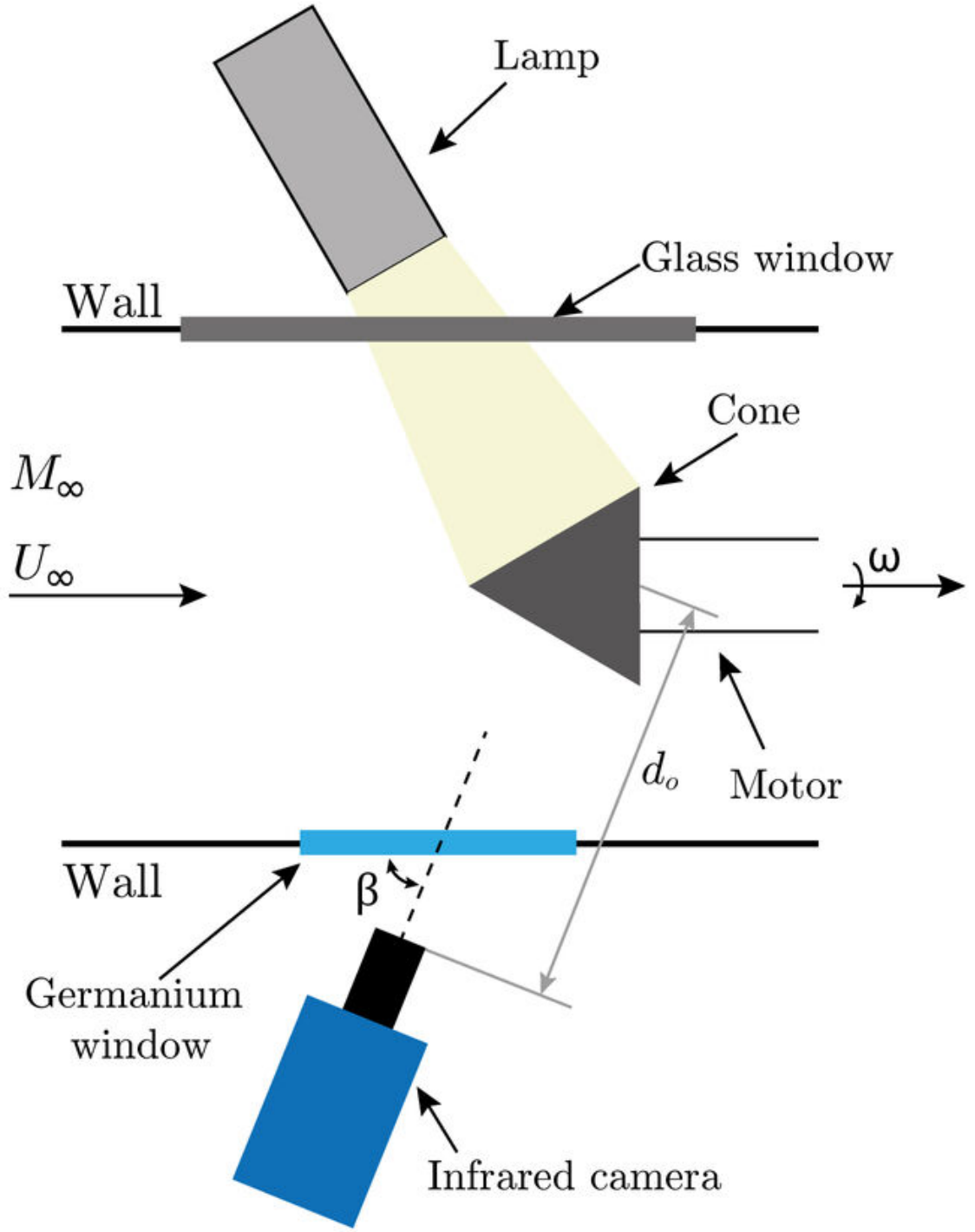
This is the author's peer reviewed, accepted manuscript. However, the online version of record will be different from this version once it has been copyedited and typeset.

PLEASE CITE THIS ARTICLE AS DOI: 10.1063/1.50083564



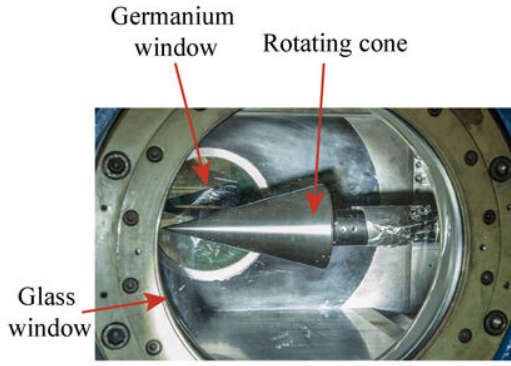
This is the author's peer reviewed, accepted manuscript. However, the online version of record will be different from this version once it has been copyedited and typeset.

PLEASE CITE THIS ARTICLE AS DOI: 10.1063/1.50083564

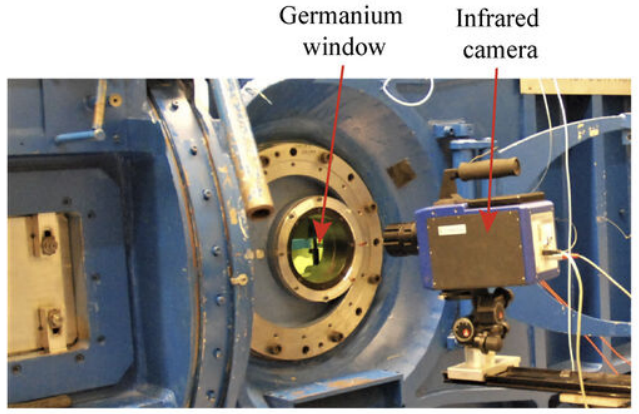


This is the author's peer reviewed, accepted manuscript. However, the online version of record will be different from this version once it has been copyedited and typeset.

PLEASE CITE THIS ARTICLE AS DOI: 10.1063/1.50083564



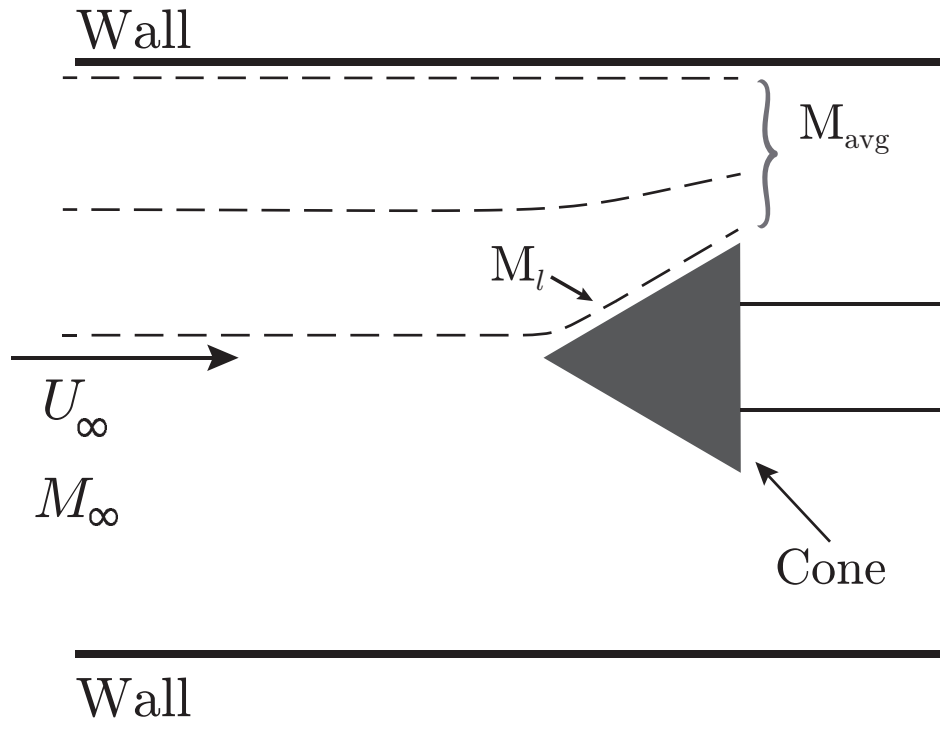
(a)



(b)

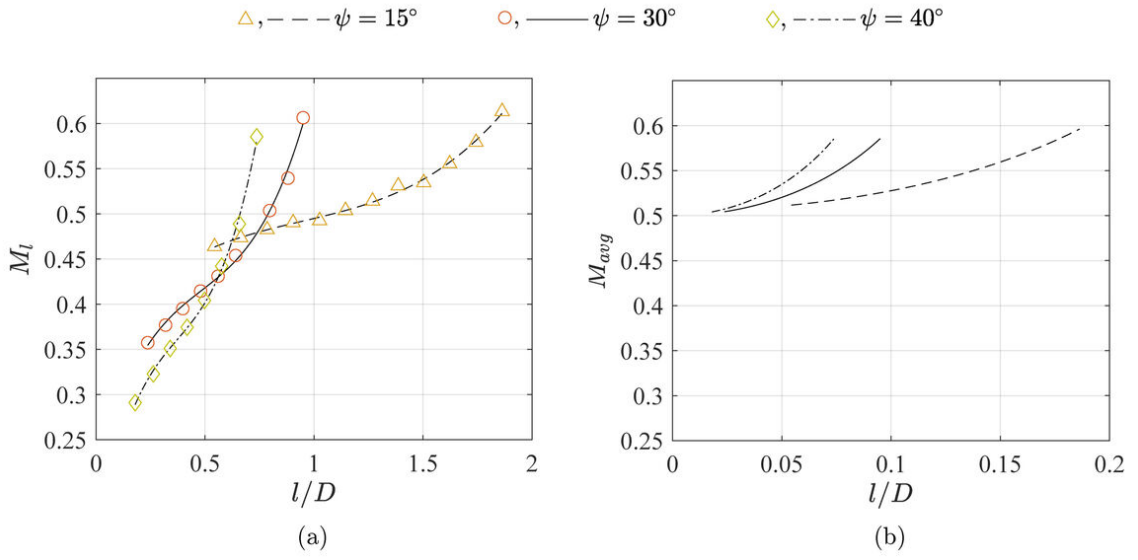
This is the author's peer reviewed, accepted manuscript. However, the online version of record will be different from this version once it has been copyedited and typeset.

PLEASE CITE THIS ARTICLE AS DOI: 10.1063/1.50083564



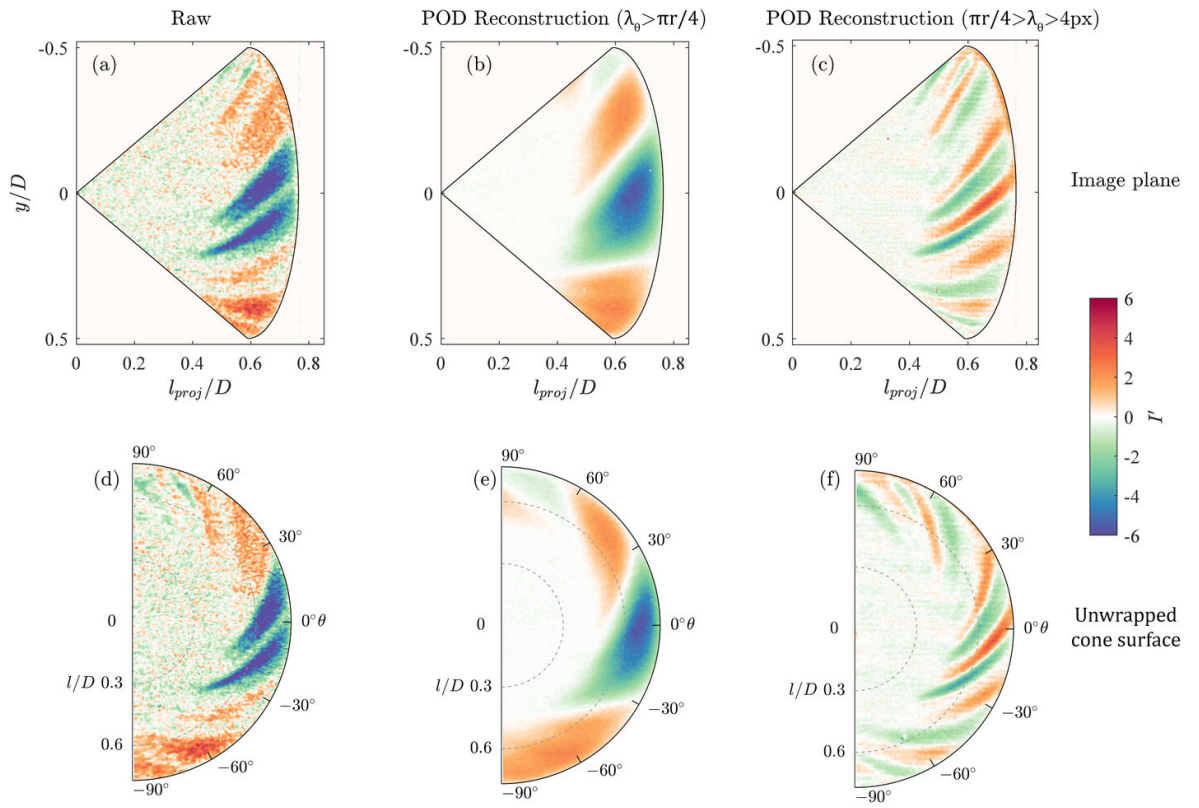
This is the author's peer reviewed, accepted manuscript. However, the online version of record will be different from this version once it has been copyedited and typeset.

PLEASE CITE THIS ARTICLE AS DOI: 10.1063/1.50083564



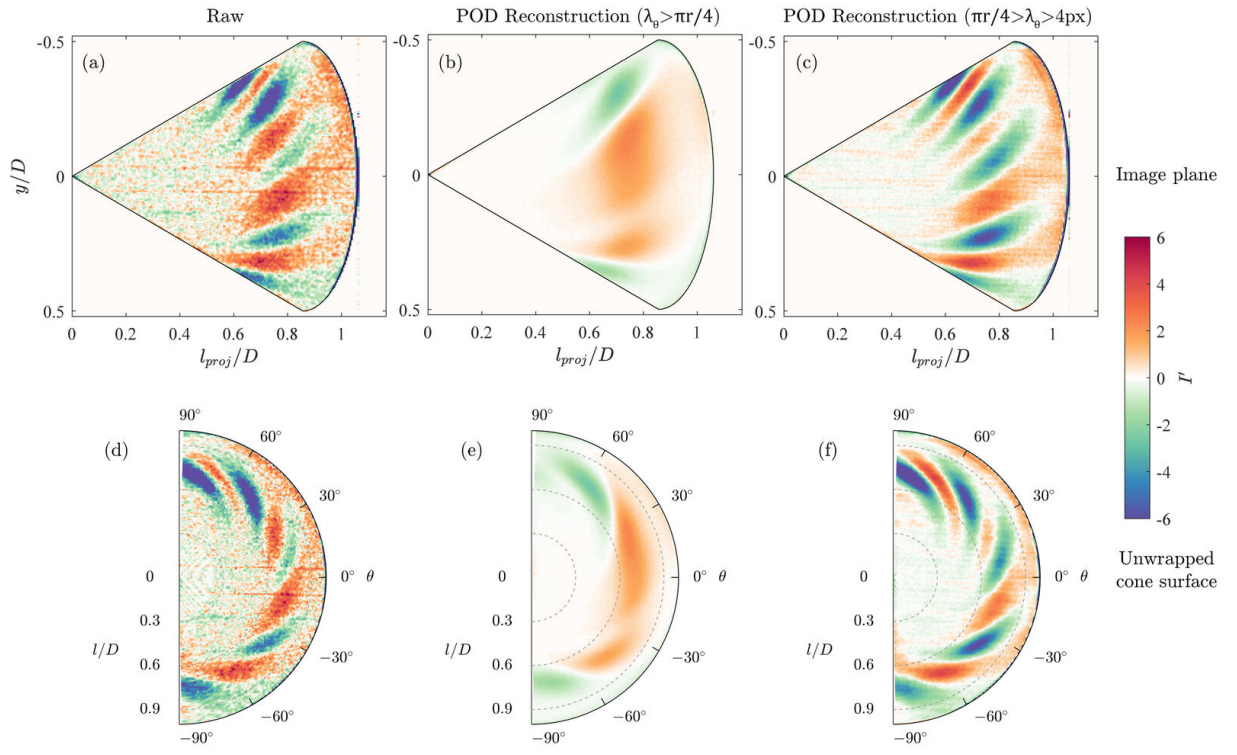
This is the author's peer reviewed, accepted manuscript. However, the online version of record will be different from this version once it has been copyedited and typeset.

PLEASE CITE THIS ARTICLE AS DOI: 10.1063/1.50083564



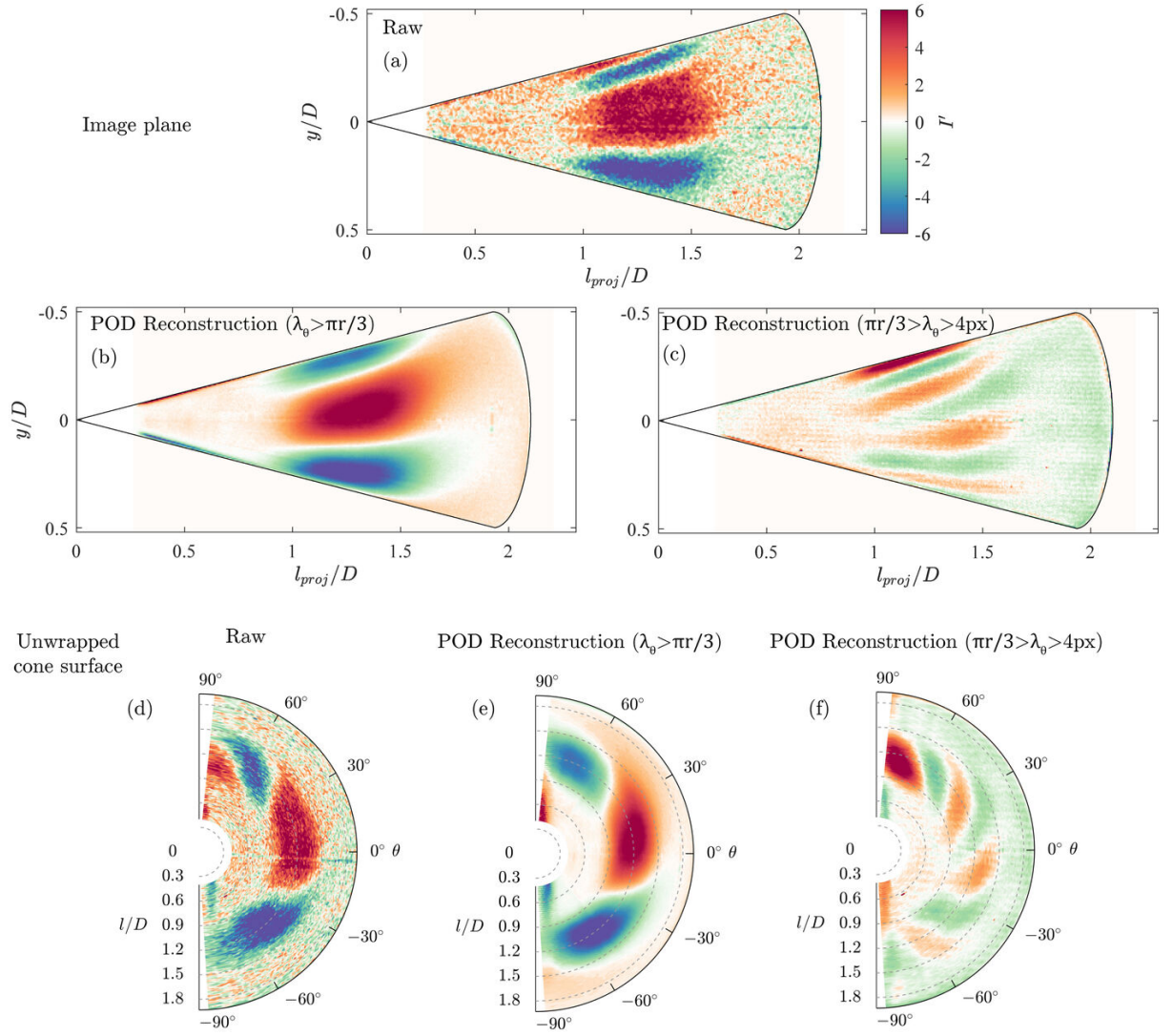
This is the author's peer reviewed, accepted manuscript. However, the online version of record will be different from this version once it has been copyedited and typeset.

PLEASE CITE THIS ARTICLE AS DOI: 10.1063/1.50083564



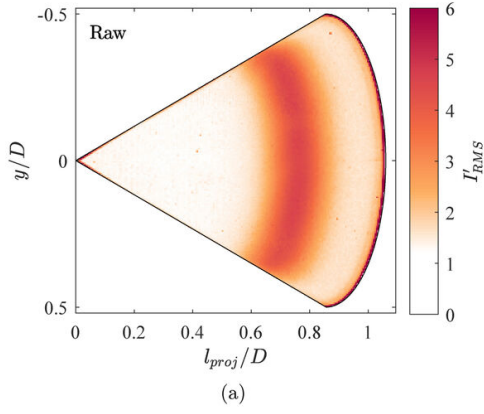
This is the author's peer reviewed, accepted manuscript. However, the online version of record will be different from this version once it has been copyedited and typeset.

PLEASE CITE THIS ARTICLE AS DOI: 10.1063/1.50083564

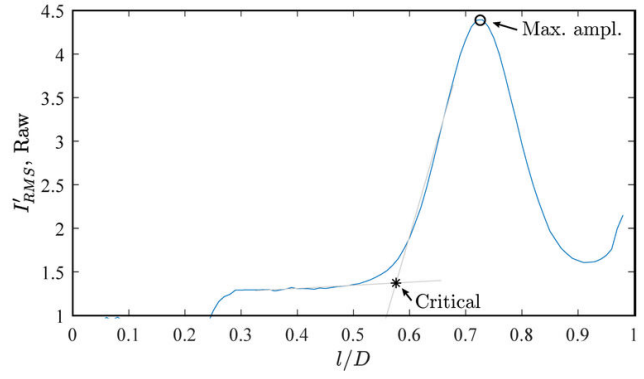


This is the author's peer reviewed, accepted manuscript. However, the online version of record will be different from this version once it has been copyedited and typeset.

PLEASE CITE THIS ARTICLE AS DOI: 10.1063/1.50083564



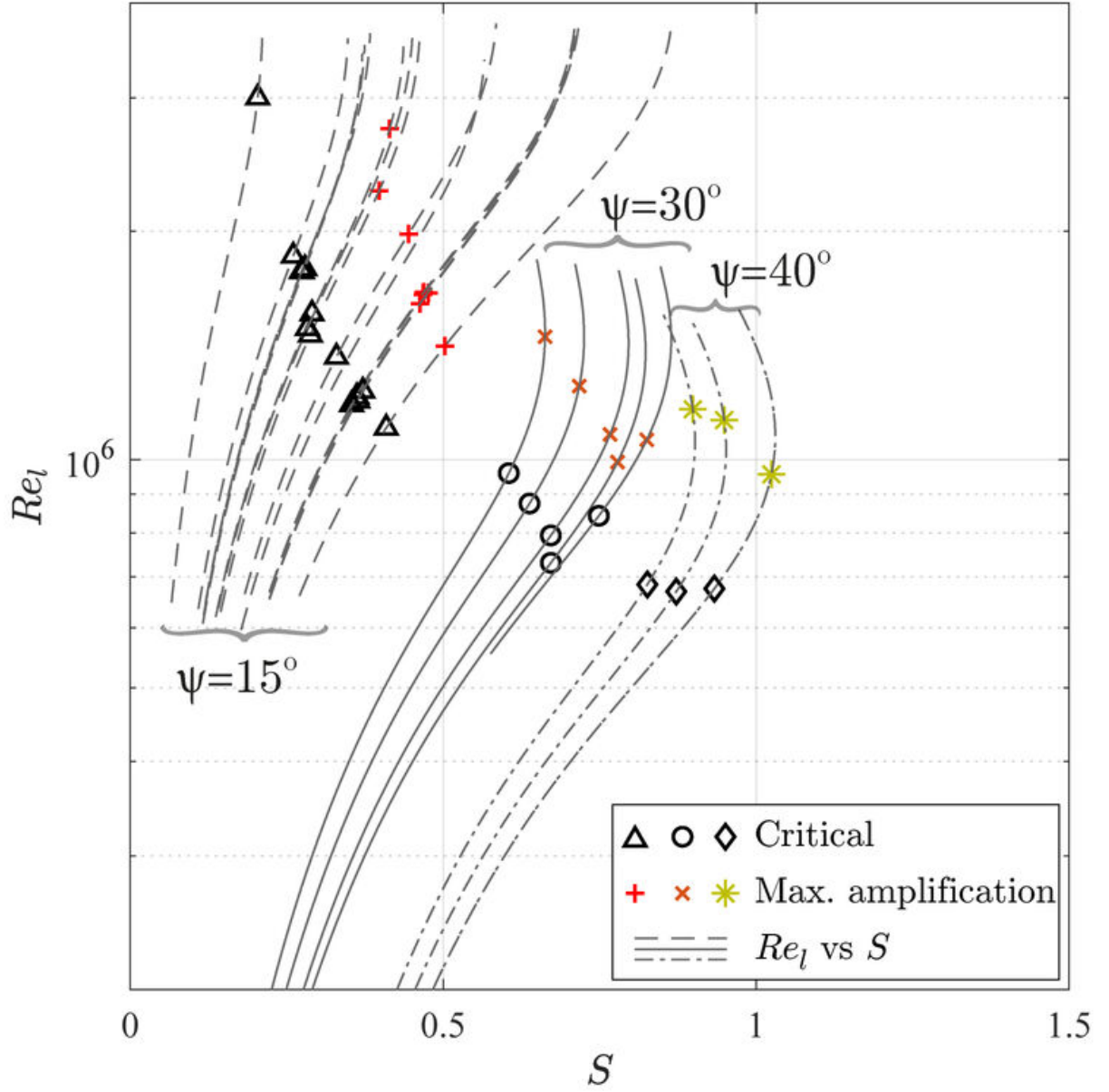
(a)



(b)

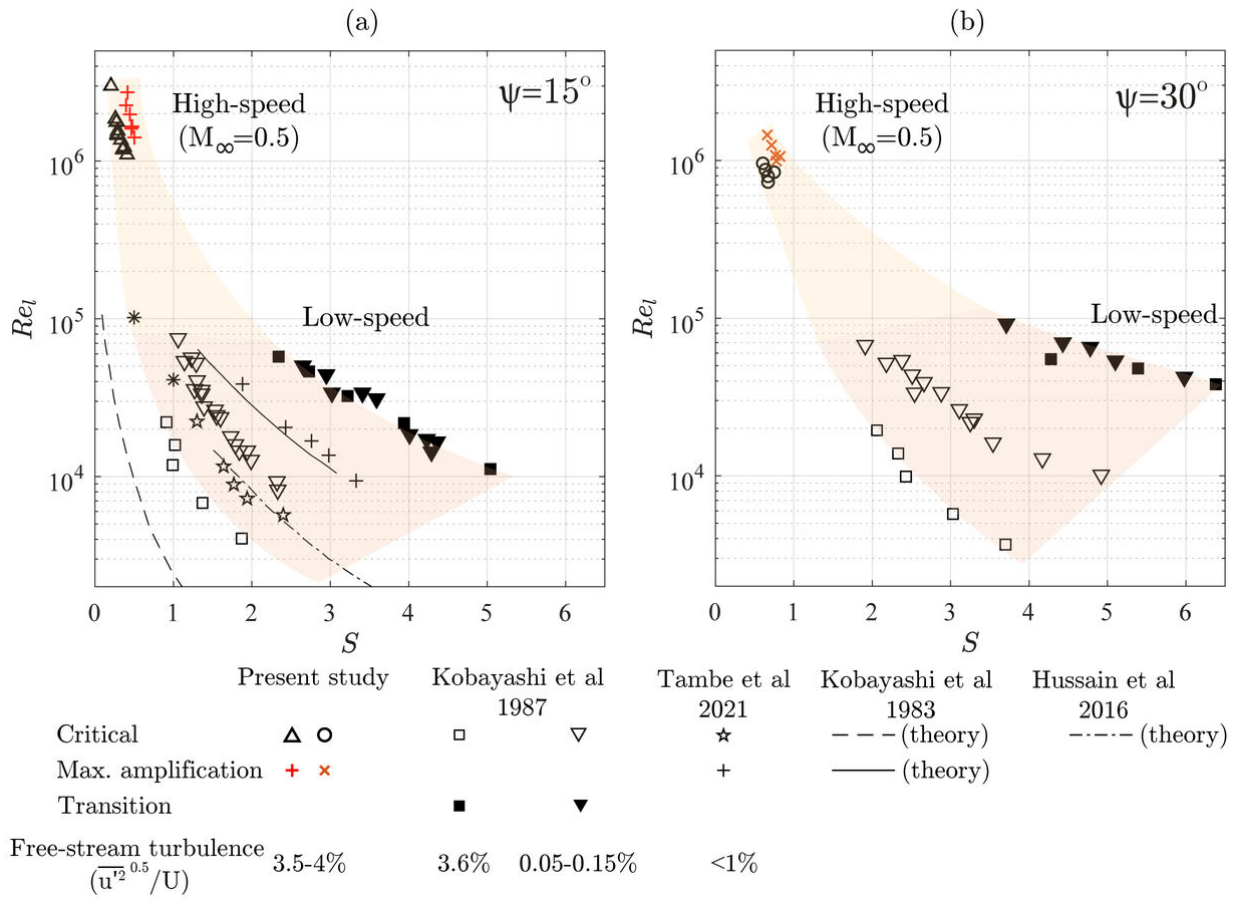
This is the author's peer reviewed, accepted manuscript. However, the online version of record will be different from this version once it has been copyedited and typeset.

PLEASE CITE THIS ARTICLE AS DOI: 10.1063/1.50083564



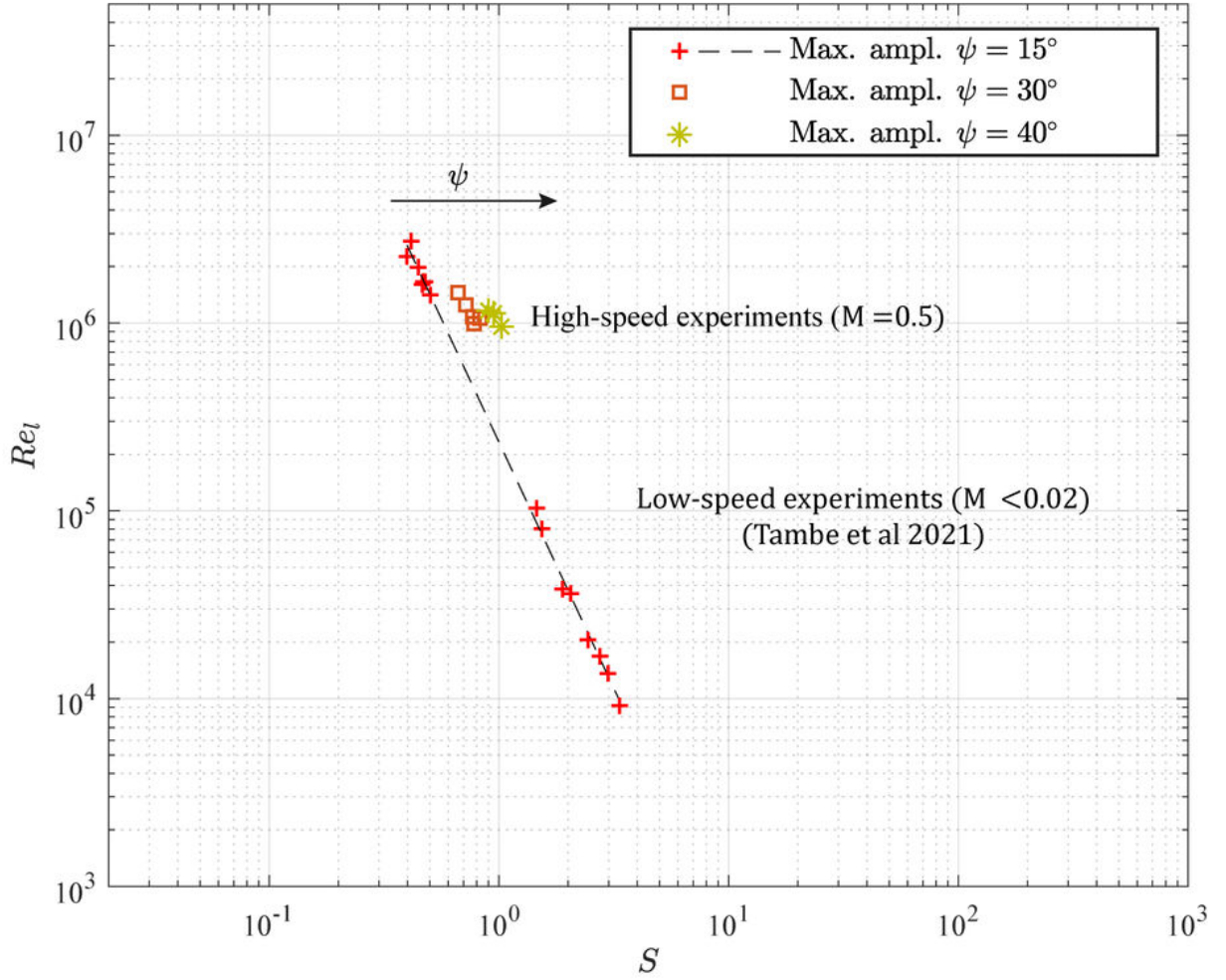
This is the author's peer reviewed, accepted manuscript. However, the online version of record will be different from this version once it has been copyedited and typeset.

PLEASE CITE THIS ARTICLE AS DOI: 10.1063/5.0083564



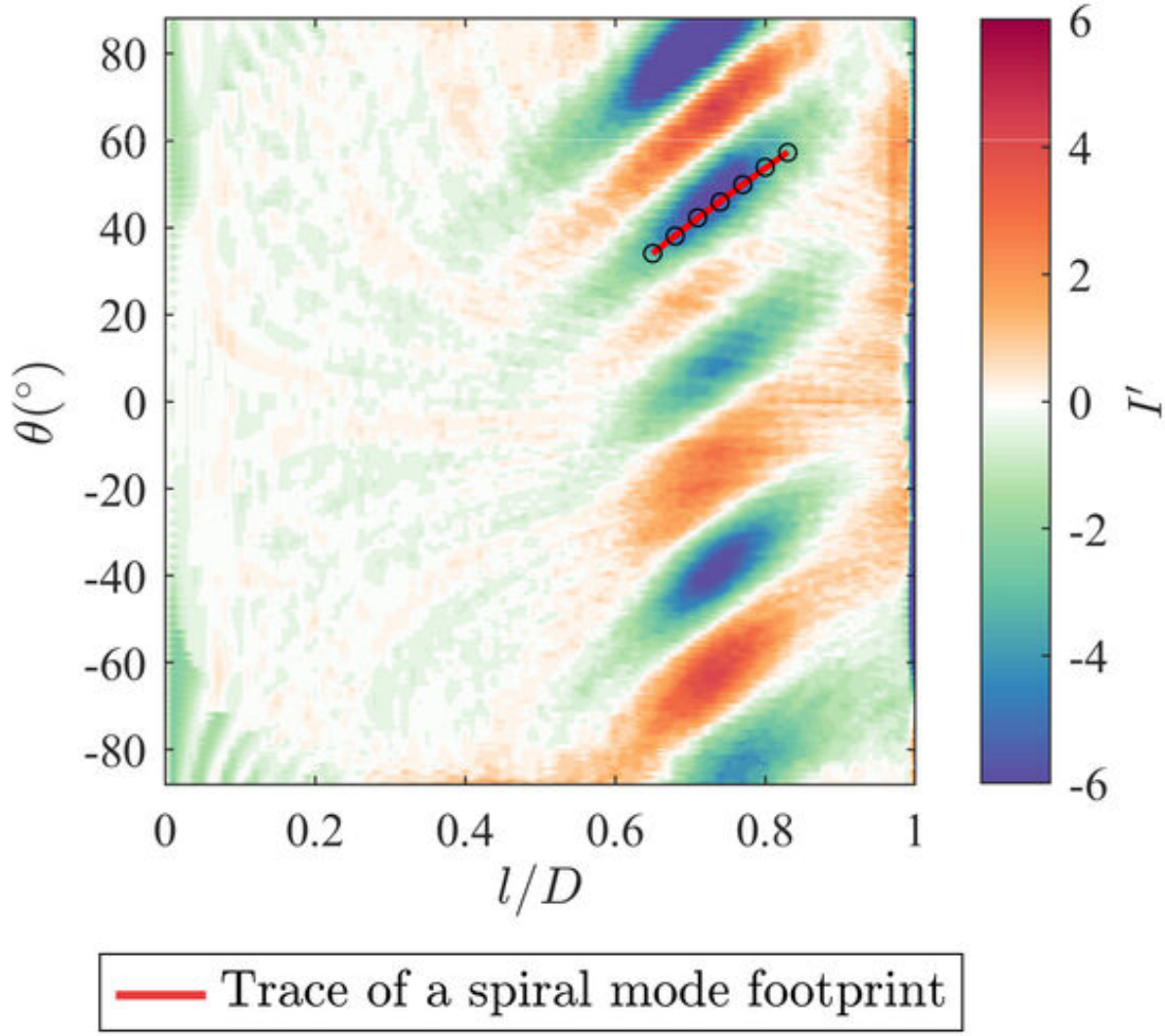
This is the author's peer reviewed, accepted manuscript. However, the online version of record will be different from this version once it has been copyedited and typeset.

PLEASE CITE THIS ARTICLE AS DOI: 10.1063/5.0083564



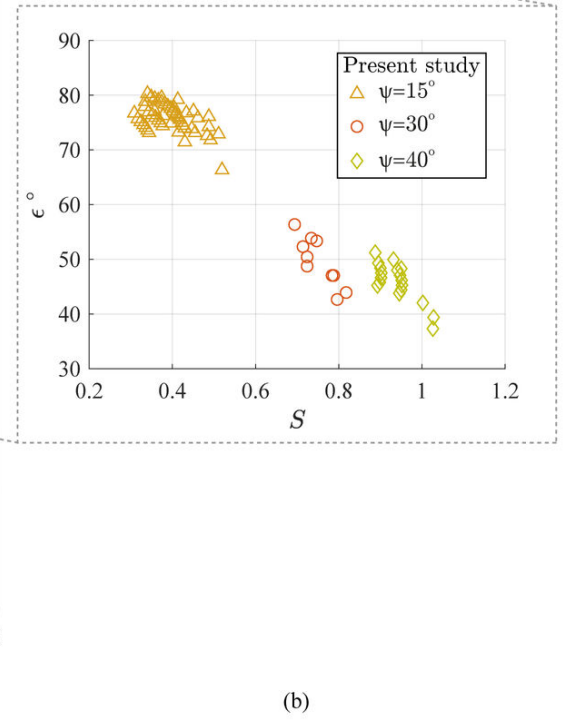
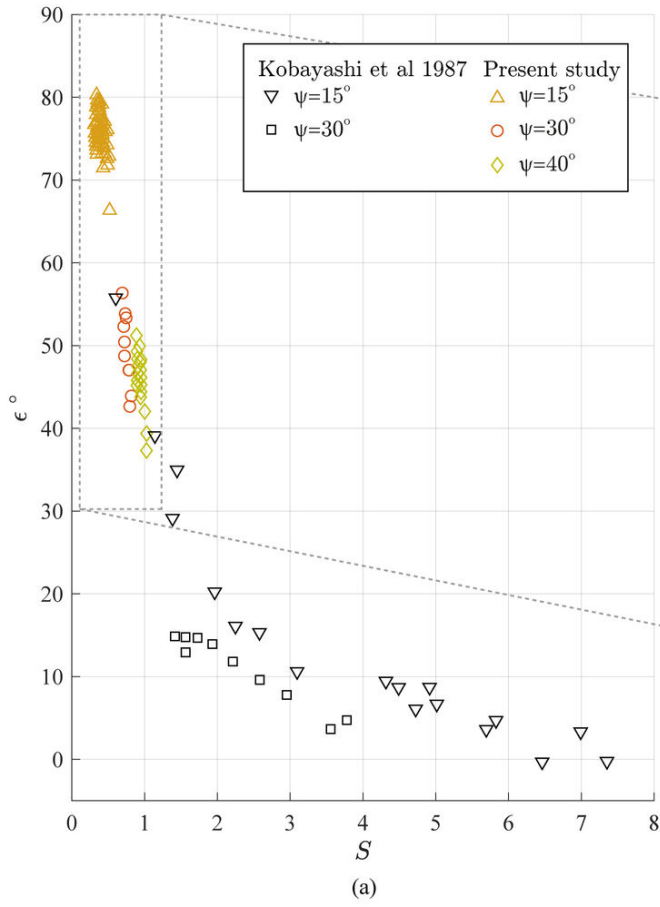
This is the author's peer reviewed, accepted manuscript. However, the online version of record will be different from this version once it has been copyedited and typeset.

PLEASE CITE THIS ARTICLE AS DOI: 10.1063/1.50083564

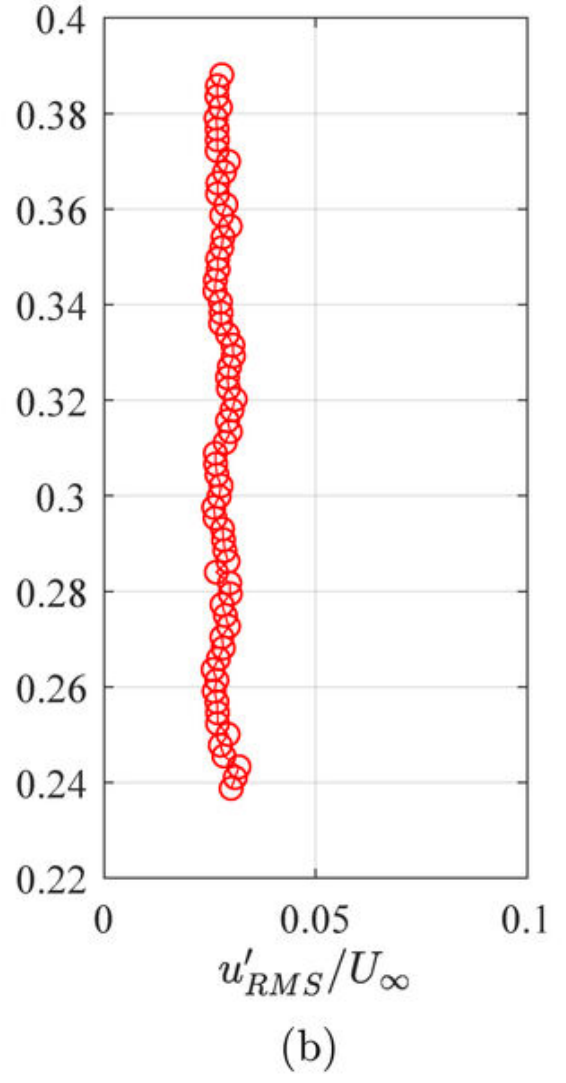
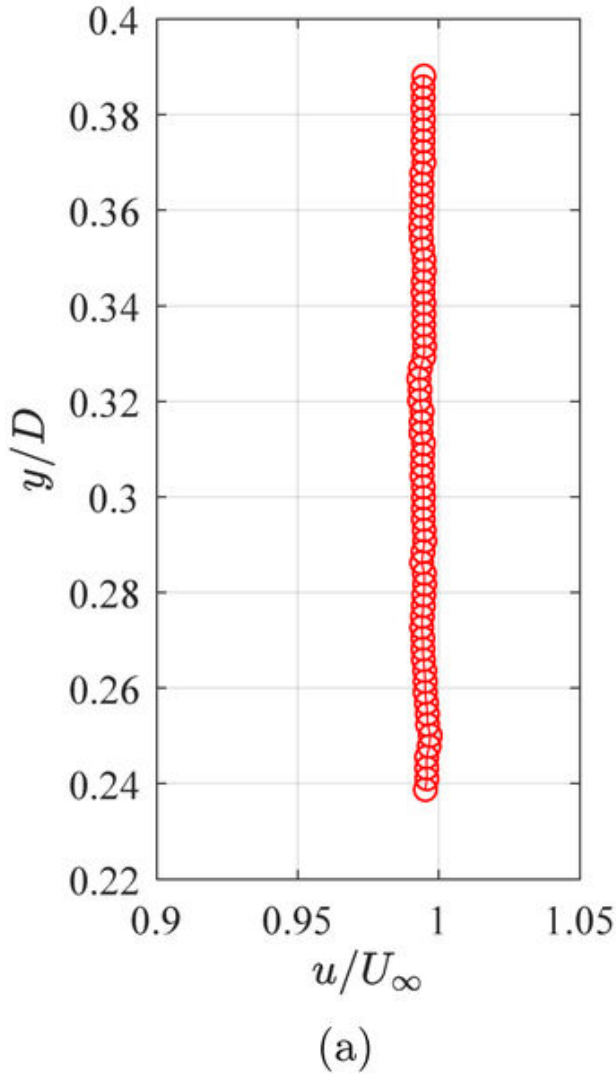


This is the author's peer reviewed, accepted manuscript. However, the online version of record will be different from this version once it has been copyedited and typeset.

PLEASE CITE THIS ARTICLE AS DOI: 10.1063/1.50083564

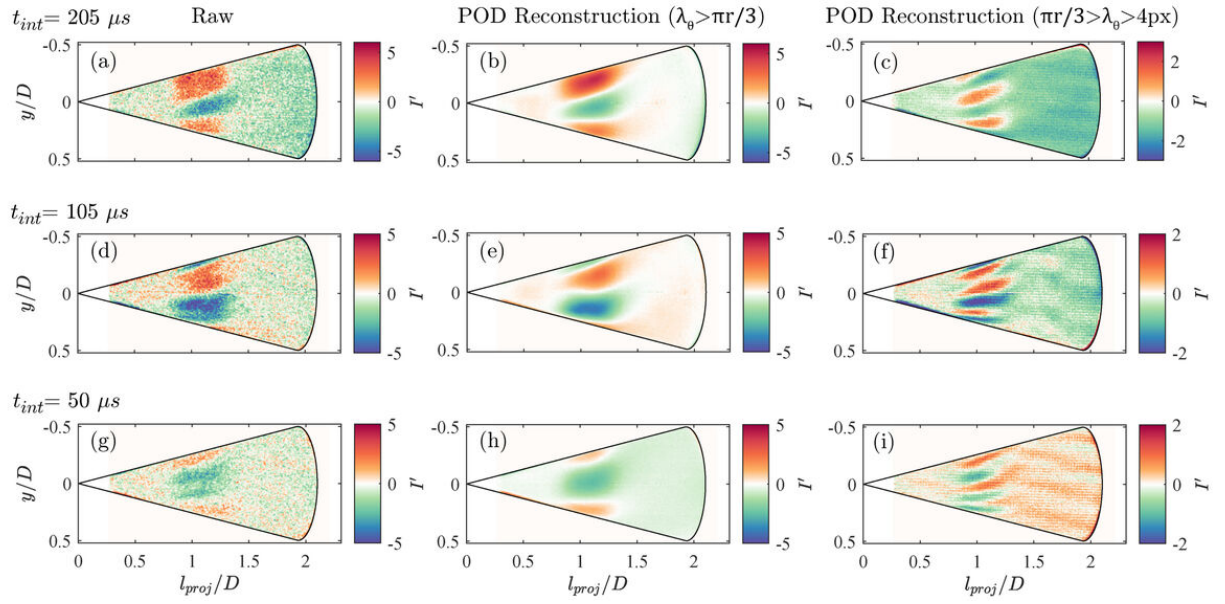


This is the author's peer reviewed, accepted manuscript. However, the online version of record will be different from this version once it has been copyedited and typeset.
 PLEASE CITE THIS ARTICLE AS DOI: 10.1063/5.0083564



This is the author's peer reviewed, accepted manuscript. However, the online version of record will be different from this version once it has been copyedited and typeset.

PLEASE CITE THIS ARTICLE AS DOI: 10.1063/1.50083564



This is the author's peer reviewed, accepted manuscript. However, the online version of record will be different from this version once it has been copyedited and typeset.

PLEASE CITE THIS ARTICLE AS DOI: 10.1063/1.50083564

